

JGR Solid Earth



RESEARCH ARTICLE

10.1029/2022JB024191

Wim Simons, Taco Broerse, and Lin Shen contributed equally to this work.

Key Points:

- New Global Positioning System observations as part of a geodetic solution for the full 3D onshore co-seismic displacements of the 2018 Palu earthquake
- Below Palu Bay we find a strong indication of dip-slip on a fault bend, agreeing with the notion of Palu Valley being a transtensional basin
- A large part of the tsunami, both in terms of arrival times and runup heights, can be explained by co-seismic slip

Supporting Information:

Supporting Information may be found in the online version of this article.

Correspondence to:

T. Broerse,
d.b.t.broerse@uu.nl

Citation:

Simons, W., Broerse, T., Shen, L., Kleptsova, O., Nijholt, N., Hooper, A., et al. (2022). A tsunami generated by a strike-slip event: Constraints from GPS and SAR data on the 2018 Palu earthquake. *Journal of Geophysical Research: Solid Earth*, 127, e2022JB024191. <https://doi.org/10.1029/2022JB024191>

Received 16 FEB 2022

Accepted 3 NOV 2022

Corrected 14 DEC 2022

This article was corrected on 14 DEC 2022. See the end of the full text for details.

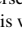











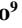

Author Contributions:

Conceptualization: Wim Simons, Taco Broerse, Nicolai Nijholt, Andrew Hooper, Julie Pietrzak, Matthew Herman, Rob Govers, Christophe Vigny

© 2022 The Authors.

This is an open access article under the terms of the [Creative Commons Attribution-NonCommercial License](https://creativecommons.org/licenses/by-nc/4.0/), which permits use, distribution and reproduction in any medium, provided the original work is properly cited and is not used for commercial purposes.

A Tsunami Generated by a Strike-Slip Event: Constraints From GPS and SAR Data on the 2018 Palu Earthquake

Wim Simons¹ , Taco Broerse² , Lin Shen³, Olga Kleptsova⁴ , Nicolai Nijholt¹ , Andrew Hooper³ , Julie Pietrzak⁴ , Yu Morishita^{5,6} , Marc Naeije¹, Stef Lhermitte^{4,7} , Matthew Herman² , Dina Anggreni Sarsito⁸, Joni Efendi⁹ , Sofian¹⁰, Rob Govers² , Christophe Vigny¹¹, Hasanuddin Zainal Abidin⁸ , Gatot Haryo Pramono⁹ , Cahyo Nugroho¹⁰, Pieter Visser¹ , and Riccardo Riva⁴ 

¹Faculty of Aerospace Engineering, Delft University of Technology, Delft, The Netherlands, ²Department of Earth Sciences, Faculty of Geosciences, Utrecht University, Utrecht, The Netherlands, ³COMET, School of Earth and Environment, University of Leeds, Leeds, UK, ⁴Faculty of Civil Engineering and Geosciences, Delft University of Technology, Delft, The Netherlands, ⁵Geospatial Information Authority of Japan, Tsukuba, Japan, ⁶Now at Synspec, Tokyo, Japan, ⁷Now at Department of Earth & Environmental Sciences, KU Leuven, Leuven, Belgium, ⁸Geodesy Research Group, Institute of Technology Bandung, Bandung, Indonesia, ⁹Center for Geodetic Control Network and Geodynamics, Geospatial Information Agency, Bogor, Indonesia, ¹⁰Meteorology, Climatology and Geophysical Agency, Jakarta, Indonesia, ¹¹Département Terre Atmosphère Océan, École Normale Supérieure, Paris, France

Abstract A devastating tsunami struck Palu Bay in the wake of the 28 September 2018 $M_w = 7.5$ Palu earthquake (Sulawesi, Indonesia). With a predominantly strike-slip mechanism, the question remains whether this unexpected tsunami was generated by the earthquake itself, or rather by earthquake-induced landslides. In this study we examine the tsunami potential of the co-seismic deformation. To this end, we present a novel geodetic data set of Global Positioning System and multiple Synthetic Aperture Radar-derived displacement fields to estimate a 3D co-seismic surface deformation field. The data reveal a number of fault bends, conforming to our interpretation of the tectonic setting as a transtensional basin. Using a Bayesian framework, we provide robust finite fault solutions of the co-seismic slip distribution, incorporating several scenarios of tectonically feasible fault orientations below the bay. These finite fault scenarios involve large co-seismic uplift (>2 m) below the bay due to thrusting on a restraining fault bend that connects the offshore continuation of two parallel onshore fault segments. With the co-seismic displacement estimates as input we simulate a number of tsunami cases. For most locations for which video-derived tsunami waveforms are available our models provide a qualitative fit to leading wave arrival times and polarity. The modeled tsunamis explain most of the observed runup. We conclude that co-seismic deformation was the main driver behind the tsunami that followed the Palu earthquake. Our unique geodetic data set constrains vertical motions of the sea floor, and sheds new light on the tsunamigenesis of strike-slip faults in transtensional basins.

Plain Language Summary The 28 September Palu earthquake ruptured the Palu-Koro fault in NW Sulawesi, Indonesia, and was followed by a devastating tsunami in Palu Bay. As the Palu-Koro fault accommodates mostly horizontal motion, many studies proposed that sub-marine landslides, rather than the earthquake itself, triggered the tsunami. This study focuses on the contribution of the earthquake to sea floor displacements. We present a unique geodetic data set and estimate a high-resolution 3D displacement field. The rupture is not a straight feature in the landscape, but rather contains bends. It is near those bends that significant vertical displacements occurred. From the onshore geodetic data we infer another fault bend below Palu Bay. Estimations of fault slip for several scenarios of offshore fault geometries point to a few meters of sea floor uplift. We use these slip models as input for tsunami models, and can qualitatively explain the observations of tsunami runup heights and video-based tsunami arrival times around Palu Bay. Only at a few locations our models cannot explain tsunami observations, which leaves open the contribution of other possible sources to the tsunami locally. The Palu case underlines the potential importance of fault bends to tsunami generation for similar tectonic settings around the world.

1. Introduction

The 28 September 2018 Palu $M_w = 7.5$ earthquake ruptured the Palu-Koro strike-slip fault in northwestern Sulawesi (USGS, 2018) (Figure 1). The event was quickly followed by tsunami waves that first arrived 2–5 min

Data curation: Wim Simons, Dina Anggreni Sarsito, Joni Efendi, Sofian, Christophe Vigny
Formal analysis: Wim Simons, Yu Morishita, Marc Naeije, Dina Anggreni Sarsito, Joni Efendi
Funding acquisition: Wim Simons, Taco Broerse, Nicolai Nijholt, Julie Pietrzak, Joni Efendi, Christophe Vigny, Pieter Visser, Riccardo Riva
Investigation: Wim Simons, Taco Broerse, Lin Shen, Olga Kleptsova, Nicolai Nijholt, Stef Lhermitte, Matthew Herman
Methodology: Taco Broerse, Lin Shen, Olga Kleptsova, Stef Lhermitte
Project Administration: Wim Simons, Joni Efendi, Hasanuddin Zainal Abidin, Gatot Haryo Pramono, Cahyo Nugroho, Pieter Visser
Resources: Wim Simons, Dina Anggreni Sarsito, Joni Efendi, Sofian, Christophe Vigny
Software: Taco Broerse, Lin Shen, Marc Naeije
Supervision: Taco Broerse, Andrew Hooper, Julie Pietrzak, Riccardo Riva
Visualization: Wim Simons, Taco Broerse, Lin Shen, Olga Kleptsova, Nicolai Nijholt
Writing – original draft: Wim Simons, Taco Broerse, Lin Shen, Olga Kleptsova, Nicolai Nijholt, Andrew Hooper, Yu Morishita, Marc Naeije, Stef Lhermitte
Writing – review & editing: Wim Simons, Taco Broerse, Nicolai Nijholt, Andrew Hooper, Julie Pietrzak, Yu Morishita, Stef Lhermitte, Rob Govers, Christophe Vigny, Gatot Haryo Pramono, Pieter Visser, Riccardo Riva

after the rupture (Carvajal et al., 2019; Takagi et al., 2019; Yalçiner et al., 2018). Tsunami waves hit the coast of Palu Bay, but areas north of the bay, along the Makassar Strait, were hardly affected (Omira et al., 2019; Yalçiner et al., 2018), even though these areas are at comparable distances to the rupture. The unexpected amplitude of the tsunami and the timing of the earthquake increased the damage and may have caused additional casualties; the earthquake occurred at sunset when many people were present on the beach, at rising sea tide (at 80% of high tide, about 0.85 m). Furthermore, there have been numerous reports of landslides directly at the coast (Liu et al., 2020; Omira et al., 2019; Takagi et al., 2019), while liquefaction-induced landslides in Palu Valley destroyed suburban areas (Bradley et al., 2019; Watkinson & Hall, 2019). From a tsunami-generation perspective, an important question quickly arose: was the tsunami a result of co-seismic displacements of the sea floor, or did secondary effects such as (sub-marine) landslides play a major role (Arikawa et al., 2018; Muhari et al., 2018)?

The Palu-Koro fault, which runs underneath the city of Palu, accommodates approximately 4 cm/yr left-lateral relative plate motion (Bellier et al., 2001; Stevens et al., 1999; Walpersdorf, Rangin, & Vigny, 1998). However, interseismically the segment at Palu Bay and Valley is locked at shallow depths (down to 12 km), as indicated by Global Positioning System (GPS)-derived velocities across the Palu-Koro fault (Socquet et al., 2006; Walpersdorf, Vigny, et al., 1998). This results in a steady accumulation of slip deficit. It was therefore clear that Palu is situated in an area with a high seismic hazard (Cipta et al., 2017; Watkinson & Hall, 2017). Geological (Bellier et al., 2006), geomorphological (Bellier et al., 1998, 2001) and geodetic observations (Socquet et al., 2006; Walpersdorf, Vigny, et al., 1998) clearly indicate that the Palu-Koro fault is an active fault system, even though seismological observations for a high-magnitude rupture are lacking (Watkinson & Hall, 2017). Pelinovsky et al. (1997) and Prasetya et al. (2001) attributed three tsunamis hitting Sulawesi's west coast over the last century to earthquakes in the Palu-Koro zone, even though the inferred source mechanisms indicated thrust and normal earthquakes rather than strike-slip.

The Quaternary activity of the prominent Palu-Koro fault is characterized in the geomorphology by very narrow, steep valleys as the fault runs through central Sulawesi (Bellier et al., 1998; Katili, 1970). The Palu-Koro fault system branches out at the surface, entering Palu Valley from the south, as it continues toward Palu Bay as a transtensional system; steep, valley-dipping normal faults bound the valley at the base of the surrounding mountain systems (Bellier et al., 1998; Watkinson & Hall, 2017). The transtensional nature of the Palu-Koro fault indicates the possibility for dip-slip components that increase vertical surface displacements during earthquakes, similar to what has been proposed for the Sea of Marmara region of the North Anatolian fault (Tinti et al., 2006). This may allow for large tsunami amplitudes during strike-slip earthquakes while the dominant motions are expected to be horizontal.

Seismological studies inferred that the $M_w = 7.5$ rupture started 72 km north of Palu (USGS, 2018), and propagated southwards at supershear velocity (i.e., faster than the shear wave velocity of the crust) (Amlani et al., 2022; Bao et al., 2019). The seismologically inferred slip type is predominantly strike-slip but with a distinct dip-slip contribution, and peak slip has been mapped close to the surface (Li et al., 2020; USGS, 2018; Yolsal-Çevikbilen & Taymaz, 2019). Optical satellite data (Socquet et al., 2019; Sotiris et al., 2018) indicate that the southern part of the rupture reached the surface, and ran parallel with the fault traces as mapped prior to the earthquake (Watkinson & Hall, 2017; Wu et al., 2020). Contrastingly, north of Palu Bay these satellite data indicate a north-south oriented rupture through the Sulawesi Neck that does not follow a previously mapped major fault, as the northern continuation of the Palu-Koro fault was thought to continue offshore (Figure 1) (e.g., Bellier et al., 2001).

Observations of the time evolution of the tsunami are sparse; there is only a single direct measurement of sea level at the tide gauge in Palu Bay, complemented by analyses from tsunami videos and interviews with witnesses (Takagi et al., 2019; Yalçiner et al., 2018). Both eyewitness accounts as well as video analyses (Carvajal et al., 2019) indicate a complex tsunami evolution, with multiple waves arriving from different directions. As an embayment like Palu Bay has the potential to produce reflected tsunami waves, it is inherently difficult to discern whether all observed tsunami fronts are generated by reflection of one major, tectonically induced tsunami, or whether multiple landslides are simultaneously producing waves. Surveys of inundation and runup heights suggest short wavelength tsunamis as runup distances are relatively short (Omira et al., 2019; Putra et al., 2019; Switzer et al., 2019). Multiple studies reported evidence for the occurrence of sub-marine landslides along the Bay coast (Arikawa et al., 2018; Omira et al., 2019; Sassa & Takagawa, 2019; Takagi et al., 2019) and debated their significance for generating tsunami waves in the bay (Pakoksung et al., 2019; Schambach et al., 2020; Sepúlveda et al., 2020; Williamson et al., 2020). Still, only for a few locations along the bay has it been possible

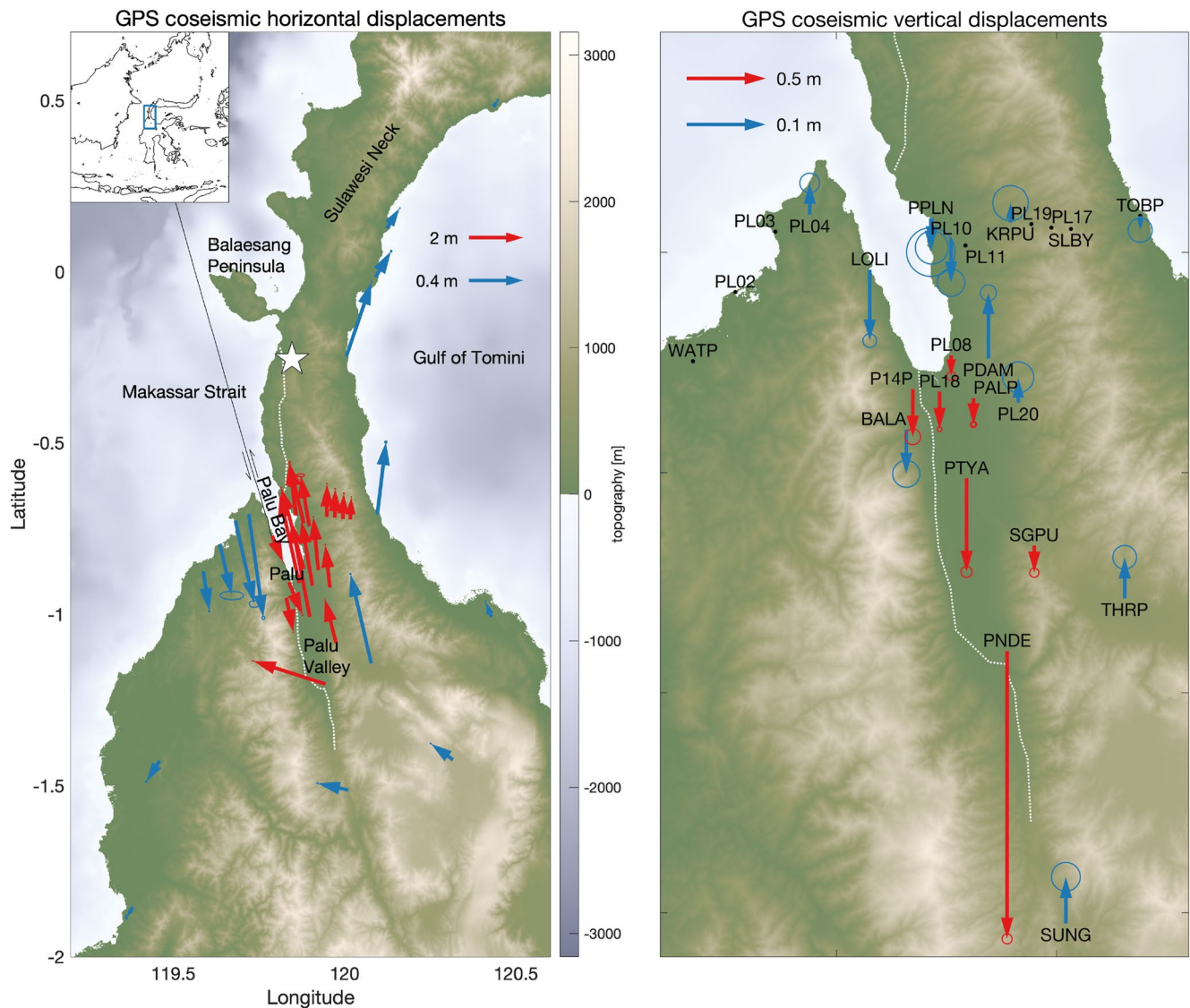


Figure 1. (Left panel) Horizontal Global Positioning System (GPS) co-seismic displacements (with 95% confidence ellipses), topography, and onshore fault traces (dotted white line) as obtained from Synthetic Aperture Radar data. The straight black line shows the continuation of the Palu-Koro fault as proposed in literature (e.g., Bellier et al., 2006), but which deviates from the 2018 surface rupture. (Right panel) Vertical GPS displacements (with 95% confidence intervals shown as circles). Vertical displacements smaller than 2σ are not shown (black dots). We use a different scaling for the large displacements (red) and small displacements (blue), see the example vectors. All co-seismic offsets can be found in Table S1 in Supporting Information S1.

to detect likely sources from bathymetry changes and put quantitative constraints on the displaced volumes (Liu et al., 2020). Many of the aforementioned studies have advocated for a dominant contribution of submarine landslides in generating the tsunami after the earthquake. Yet, due to a lack of accurate geodetic constraints, such as co-seismic GPS displacements, the offshore co-seismic displacement and its impact on generating tsunami waves have not been well constrained. The open question is still: can we find a geologically acceptable faulting model that agrees with observed surface deformation, and that also reproduces the tsunami observations without additional landslides?

To answer this question, we present a novel data set of co-seismic GPS displacements combined with a large set of Synthetic Aperture Radar (SAR) pixel offsets and SAR interferometry (InSAR) to resolve simultaneously the near and far field surface displacements associated with the M_w 7.5 Palu earthquake. Our combination of geodetic observations yields improved constraints on the co-seismic 3D displacement field; especially the vertical surface motions are much more accurate compared to previous studies that relied on InSAR or optical correlation

displacements only (Fang et al., 2019; Jamelot et al., 2019; Sepúlveda et al., 2020; Socquet et al., 2019; Ulrich et al., 2019; Williamson et al., 2020). Incorporation of GPS displacements resolves the biases and trends that are typical for SAR-derived displacement fields. Furthermore, our use of 12 different solutions for SAR pixel-offsets, InSAR and multiple aperture InSAR (MAI) from five different orbit pairs mitigates the displacement direction ambiguity that results from the projection of 3D displacement on a single line-of-sight direction. Using this extensive set of geodetic data, we estimate a robust finite fault solution of the co-seismic slip distribution in a Bayesian inversion. As parts of the fault run below Palu Bay, these are only observed indirectly. Hence, we test multiple scenarios of tectonically feasible orientations of fault segments running below the bay. We then perform forward tsunami models based on the finite fault scenarios, and examine those against the available tsunami timing and runup height observations. Thereby, our study aims at providing a better view on the role of co-seismic sea floor displacements in driving the devastating tsunami in Palu Bay.

2. Data

2.1. GPS Network

Since the first campaign-style GPS surveys in Sulawesi for the 1994–1998 time window (Wilson et al., 1998), TU Delft and ENS, in corporation with the Badan Informasi Geospasial (BIG) and Institut Teknologi Bandung, have gradually densified the GPS monument network to ~40 data points around the Palu-Koro fault and in North Sulawesi. The campaign stations have been surveyed on a yearly basis, and there are five continuous stations near the Palu-Koro fault. Before, during and after the $M_w = 7.5$ earthquake all five continuous GPS stations near the Palu-Koro fault were operational, collecting data at 30 or 1 s intervals. Many of the GPS points had been surveyed less than a year earlier in campaign-style, including 4 GPS points in Palu surveyed just 1.5 months prior to the earthquake. In the following 2–5 weeks after the earthquake, all available GPS campaign points (35) were re-surveyed for at least 3 full days. Figure 1 shows the co-seismic displacements, computed using (a) high-rate kinematic GPS solutions (for continuous GPS with large displacements), (b) by differencing solutions spanning 12 days before and 12 days after the earthquake (for continuous sites with smaller displacements), and (c) by differencing multi-day averaged positions with extrapolated pre-earthquake positions corrected for linear velocities (campaign sites). Section S2 in Supporting Information S1 provides technical details, and all co-seismic offsets can be found in Table S1 in Supporting Information S1.

2.2. SAR Data Processing

We apply InSAR, MAI, and pixel-offset tracking to ALOS-2 SAR data in the L-band frequency range, to obtain a detailed co-seismic surface deformation field. The post-earthquake SAR data were acquired between 4 and 27 days since the event (see Table S3 in Supporting Information S1), using 5 different orbit pairs. L-band SAR data is much more suitable than C-band for a vegetated area like Sulawesi, in terms of coherence (e.g., Rosen et al., 1996). Each of these techniques observes different components of the displacement field, and has its own strengths and weaknesses. InSAR reveals line-of-sight deformation with high precision, but it has almost no sensitivity to deformation in the north-south direction, due to a near-polar orbit. Furthermore, InSAR tends to be decorrelated in the areas of large displacement; as Figure 2 shows, there are gaps for InSAR for most areas adjacent to the rupture, both in the Sulawesi Neck and Palu Valley. In contrast, MAI gives displacement along track and is mostly sensitive to deformation in the north-south direction, although its precision is lower than that of InSAR (Bechor & Zebker, 2006; Jung et al., 2009). Pixel-offset tracking has a lower precision still, but provides estimates of deformation in both the line-of-sight and along-track directions, even in areas of large deformation (Michel et al., 1999; Tobita et al., 2001). We use a pair of ScanSAR images and four pairs of Stripmap images to cover the whole deformation area from both ascending and descending orbits (Table S3 in Supporting Information S1). We downsample the processed SAR-derived data set using quadtrees (Decriem et al., 2010) and estimate errors for each data set by computing 1-D semivariograms (Bagnardi & Hooper, 2018) over the non-deforming regions (see Section S3.1 in Supporting Information S1). The lower panel of Figure 2 shows the different levels of uncertainty of the used SAR products, which also agree well with the level of misfit with the (projected) GPS observations. Combined, these SAR products provide a complete view of the 3D co-seismic displacement field. Lower precision techniques prove useful as these cover the regions with large displacements on the order of meters, near the surface rupture, where InSAR lacks a solution.

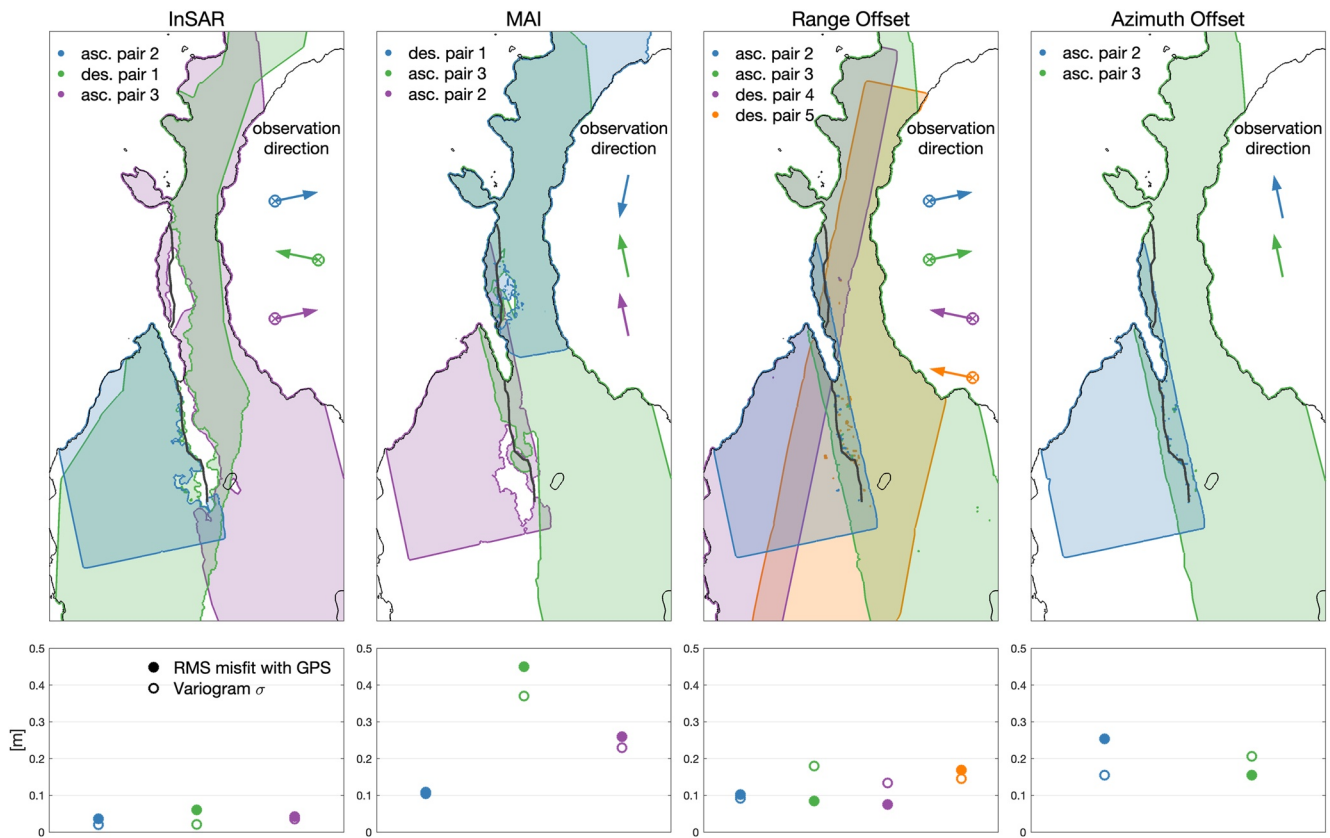


Figure 2. Synthetic Aperture Radar (SAR) data availability: areas covered by displacement fields from SAR interferometry (InSAR), multiple aperture InSAR, and SAR range and azimuth offsets (asc: ascending orbits; des: descending orbits). Table S3 in Supporting Information S1 provides details on the ALOS-2 data used. The arrow indicates the observation direction, where $a \otimes$ denotes a vertical component (down looking) for InSAR and range offsets. The dark gray line depicts the surface trace. The lower panels indicate: the respective misfits with spatially overlapping Global Positioning System (GPS) data, projected onto the same looking direction as the SAR data, and after removing an estimated offset ramp for the SAR fields, and the estimated standard deviation error, calculated for the SAR displacement field using semivariograms. We have estimated semivariograms for each SAR displacement field in areas unaffected by co-seismic displacements, hence the semivariogram standard deviation σ should be indicative for the noise level of each SAR product. For the computation of the root mean square (RMS) misfit with the GPS data, misfits larger than 2 times the RMS are removed as outliers. Figure S13 in Supporting Information S1 shows all SAR-derived displacement fields.

2.3. Estimation of 3D Displacements

The multiple SAR-derived displacements fields have highly complementary sensitivities to all directions of the displacement field, but are difficult to interpret simultaneously. Therefore, we estimate a continuous 3D displacement field from the SAR displacement fields to combine the different looking directions, while the GPS data serve to remove offsets and linear trends in the SAR displacements. We invert for the north, east and up displacements and linear trends in the SAR displacements unrelated to the co-seismic deformation, on a triangular mesh in a single linear least squares inversion, similar to Wang and Wright (2012). To incorporate the SAR fields in the inversion, we construct Green's functions that relate surface displacement to the SAR observation direction (Wright et al., 2004). We increase the local influence of the GPS data using spatial smoothing, by including a Laplacian operator in the inversion. The variable mesh size follows the spatial variability of the SAR displacements, and as we apply the same amount of smoothing between all neighboring mesh elements, the relative smoothing is dominated by the spatial variability of the SAR displacement fields. In this way we make optimal use of the SAR spatial resolution. In Section S4 in Supporting Information S1 we provide details on the inversion procedure, the effect of smoothing, and on the propagation of data uncertainties.

2.4. Displacement Field

The combination of SAR and GPS data provides a consistent co-seismic displacement field, as depicted in Figure 3, with residuals generally on the order of the data uncertainties (Figure S8 in Supporting Information S1).

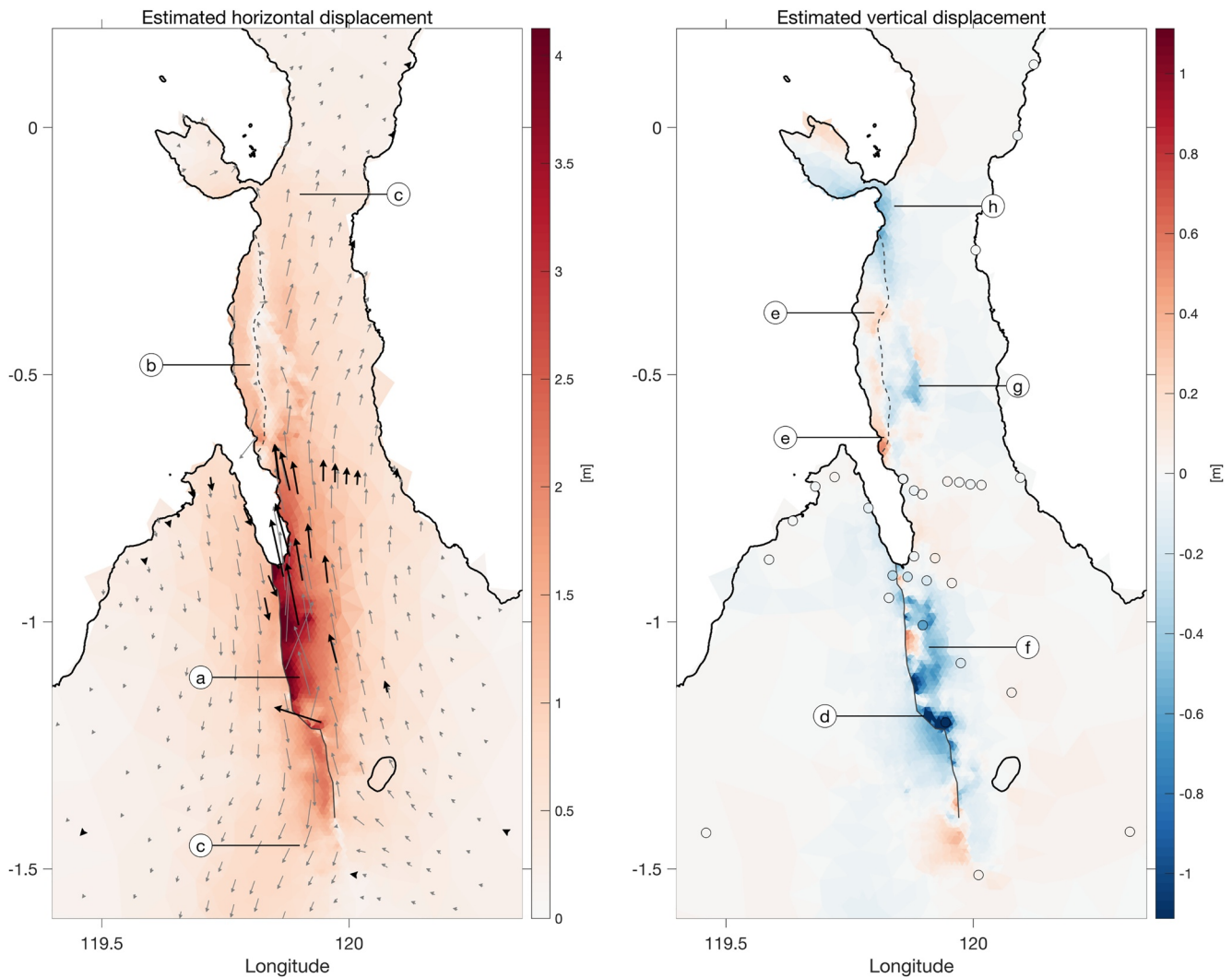


Figure 3. Estimated surface displacements, inverted from Synthetic Aperture Radar (SAR) and Global Positioning System (GPS) displacements. (Left panel) Horizontal displacements, with observed GPS vectors in black. (Right panel) Estimated vertical displacements, with uplift defined as positive. Circles denote GPS sites, where the color shows the observed vertical displacements. Black continuous line shows the surface rupture in Palu Valley, the dashed line shows the presumed surface trace north of the bay, following the gradual transition from southwards to northwards deformation. Notable features: (a) sharp transition in north-south displacements in Palu Valley; (b) smooth transition in north-south displacements showing an absence of localized surface rupture; (c) east-west displacements consistent with the ends of a left-lateral strike-slip rupture; (d) subsidence at a southern releasing fault bend; (e) uplifting areas consistent with compressional fault bends; (f) general subsidence in Palu Valley; (g) displacements suggesting normal faulting parallel to the main rupture; (h) subsidence at the west coast of the Sulawesi Neck. Figures S4 and S5 in Supporting Information S1 contain the uncertainties of the displacement fields. We fit the GPS displacements well within the observation uncertainties, see Figure S6 in Supporting Information S1.

We find good signal-to-noise ratios for the north and east displacements in the area of interest, and for the vertical displacements around the faults (see uncertainties in Figures S4 and S5 in Supporting Information S1, that also show north and east displacements separately). Approximately north-south displacements along the main Palu fault are the dominant motions; the largest displacements occurred on the east side of the fault in Palu Valley, see label (a) in Figure 3. The displacement field shows a sharp discontinuity south of the Bay, with several meters of displacement east of the surface break, suggesting extensive shallow slip along the Palu Valley rupture segment. On the other hand, we find a gradual gradient in the left-lateral motion north of the Bay (b) up to the epicenter (mostly informed by the SAR azimuth offsets and MAI, see Figure S13 in Supporting Information S1). Fault-perpendicular horizontal motions at the lateral ends of the rupture (c) indicate the expected quadrupole pattern of left-lateral slip, with minor patches of eastward motion east of the fault in Palu Valley (Figure S4 in Supporting Information S1). The near-field vertical displacements are small in general, on the order of a few tens of cm. Only around the restraining fault bend (d) in southern Palu Valley co-seismic subsidence exceeds 1 m, next

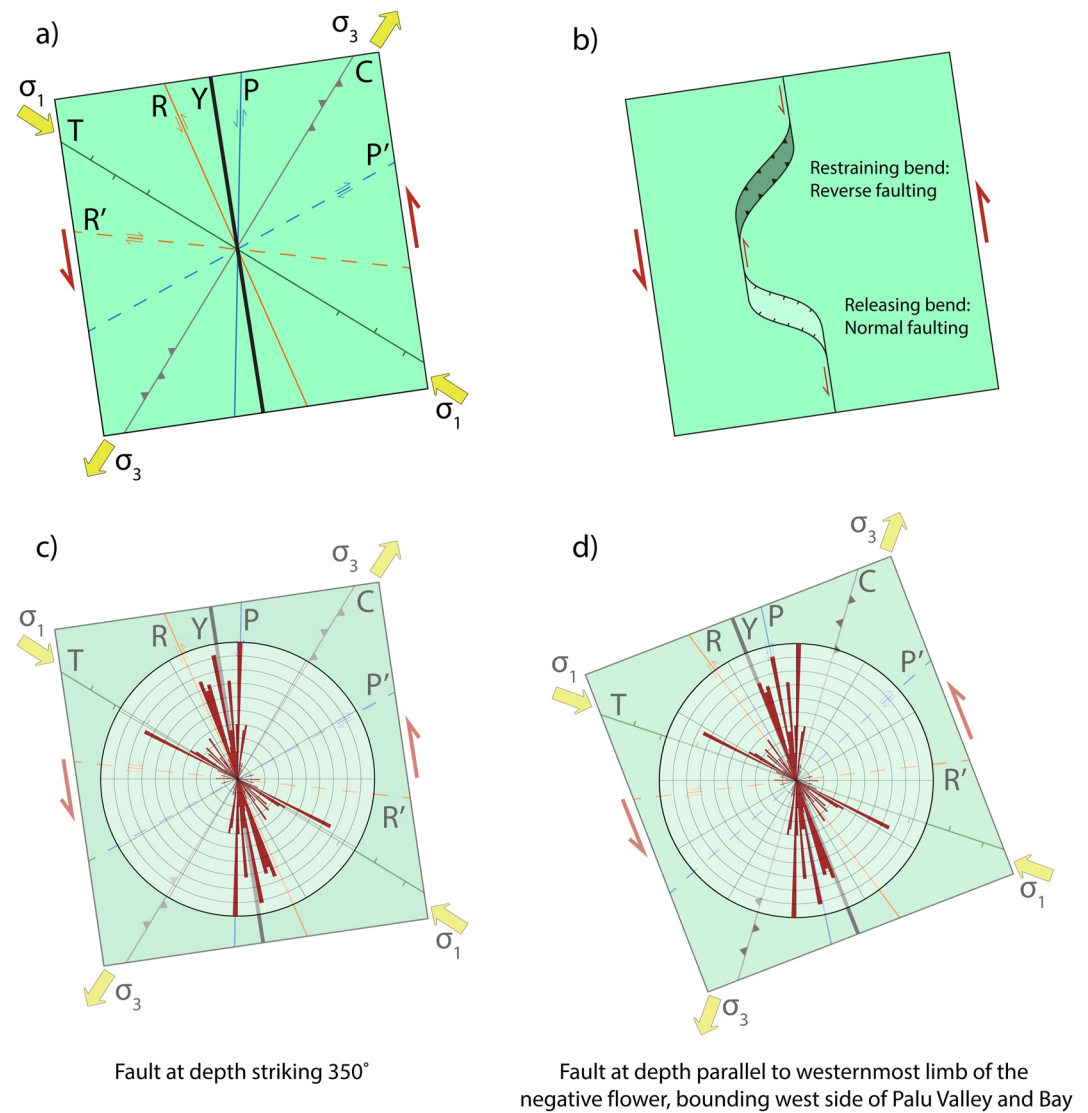


Figure 4. Interpretation of fault strikes in the 2018 rupture area as Riedel shears. (Upper left) Schematic illustration of subsidiary faults in a left-lateral shear zone. With respect to an underlying main shear zone or fault (Y), Riedel shears form at fixed orientations: $\sim 15^\circ$ for R shears, and $\sim 75^\circ$ for R' shears (Tchalenko, 1970). The minor P and antithetic P' shears are oriented approximately symmetric across the main fault compared to the R and R' shears. Tensional (T) and compressive (C) faults arise perpendicular to the positive (σ_3) and negative (σ_1) horizontal stress directions, respectively. (Upper right) Schematic illustration of azimuthal bends of the main fault in the along-strike direction. Relative motion causes a releasing bend with normal faulting and basin formation, or a restraining bend with reverse faulting (i.e., thrusting) and local uplift (Crowell, 1974). (Lower left) Rose diagram of the strikes of the active fault trace from the 2018 rupture and other features in the structural geology of the Palu-Koro fault region (Bellier et al., 1998, 2006; Hennig et al., 2017; Jaya et al., 2019; Leeuwen & Muhardjo, 2005; Natawidjaja et al., 2020; Watkinson & Hall, 2017) overlying the Riedel shear system of a main fault striking $\sim 350^\circ$. (Lower right) The same rose diagram overlying a system of Riedel shear fault orientations where the main fault runs parallel to the easternmost limb of the negative flower structure (i.e., approximately parallel to the western coast of Palu Bay, striking $\sim 340^\circ$).

to the location where Jaya et al. (2019) have observed the largest vertical offsets along surface ruptures. Similarly, we find local areas with uplift at the locations where we infer right-stepping fault bends in the Sulawesi Neck, north of the Bay (e). For a left-lateral fault system, the subsidence is in agreement with extension on a dilatational (releasing) fault bend while the uplift agrees with compressional (restraining) fault bends (Oglesby, 2005). For a graphical explanation of restraining and releasing fault bends, see Figure 4. Around Palu City we observe only small subsidence values on the order of ~ 20 cm (e.g., site *PL18*, see Table S1 in Supporting Information S1), and this general subsidence of a few decimeter applies to most of Palu Valley (f). Subsidence and NNW motion in the

Sulawesi Neck (g) suggest normal faulting east of the main fault. Around the northern end of the onshore part of the fault (h) we obtain widespread subsidence.

3. Transtension in the Palu-Koro Fault Region of NW Sulawesi

3.1. The Tectonic Setting of Palu Valley and Bay

The Palu-Koro fault is a mature strike-slip fault as it has accommodated up to 150–250 km of left-lateral motion since the end of the Miocene (Bellier et al., 2006; Walpersdorf, Rangin, & Vigny, 1998). Mature strike-slip faults commonly display complex structural features in the upper crust overlying a single, strike-slip fault at depth, where the surface fault is highly segmented (Klinger, 2010), thereby deviating from the concept of a single fault plane cutting the entire lithosphere (Tchalenko, 1970). Indications that the Palu-Koro fault is structurally complex are: (a) the maturity of the fault system, evidenced by the rectilinear geometry of the Palu Valley and Bay (graben-like) depression, sitting in between two mountain ranges with peaks >2 km (Abendanon, 1915; Katili, 1970), (b) the presence of large vertical offsets on steep valley-dipping faults, which display notable strike-slip displacements (Bellier et al., 1998; Katili, 1970; Patria & Putra, 2020; Watkinson & Hall, 2017), (c) an onshore releasing bend (indicated by *d* in Figure 3), as well as an offset between the fault trace north and south of the bay during the co-seismic rupture.

We take these geological observations into account when considering a co-seismic slip distribution on a finite fault plane, as the geometry of the ruptured fault is subject to uncertainties. Namely, the observed surface deformation field (Figure 3) is only constrained on land, and therefore cannot be directly used to understand the change in bathymetry that generated the tsunami. The geology of comparable fault settings suggests that the offset between the fault trace north and south of the bay may be due to a fault bend inside the bay (Cunningham & Mann, 2007). We aim to develop a physical fault model that reproduces the observations plus the seismic moment tensor. Surface faulting does not necessarily continue in the subsurface with the same fault orientation, so that we need to tailor our finite fault model to the tectonic setting of Palu Valley and Bay. Lacking direct seismic profiles across the Palu-Koro fault, we consider fault structures in similar geological settings worldwide.

Often, strike-slip faults are characterized by a system of continuously developing Riedel shear faults at the surface, rather than a single straight fault trace (Tchalenko, 1970). The upper left panel of Figure 4 shows such a generic set of subsidiary faults that accommodate strain within a fault zone. Such a set is comprised of subsidiary faults that accommodate strain within the fault zone, and is comprised of several fault types (R, R', P, T, C) with distinct orientations and relative motions with respect to the main fault/shear zone at depth (Y). Figure 4, upper right panel, displays the potential development of releasing bends (resulting in extension due to normal faults) or restraining bends (resulting in shortening due to reverse faults) in case the main fault trace locally changes strike (Crowell, 1974).

Releasing bends can lead to the formation of a transtensional basin, where faults may form a negative flower structure when observed in a vertical cross-section (Harding, 1985). The subsiding basin that centers the shallow section of the negative flower structure is bounded by faults that dip steeply at the surface. The relative displacement on these faults can be both normal and strike-slip. Following Bellier et al. (2006), we interpret the Palu valley and basin as transtensional, based on the presence of steep faults that bound its interior as well as on the occurrence of both strike-slip and normal faulting. Opposite present-day rotation at both sides of the Palu-Koro fault can explain the extension in the Palu basin (Socquet et al., 2006). For the faults within a negative flower structure, the dip angle changes with depth, such that faults that are parallel at the surface converge at depth to a sub-vertical, deeper main fault (Harding, 1985). Previously, Watkinson and Hall (2017) argued for such a straight, cross-basin fault at depth for Palu Valley. Various splay faults thus reach the surface from a single, buried, main fault that is continuous at depth, whilst the shallow architecture of a transtensional basin may be very complex (Aksu et al., 2000; Laigle et al., 2008). We summarize in Figure 5 our interpretation of the Palu-Koro fault as a transtensional basin, characterized by a negative flower structure in the Palu Valley and Bay region.

3.2. Interpretation of Fault Orientations as Riedel Shears

Surface-breaking faults of a negative flower structure do not have to trace the strike of buried main faults in transtensional basins strictly, as is the case in the Sea of Marmara (Aksu et al., 2000; Laigle et al., 2008; Yalçiner

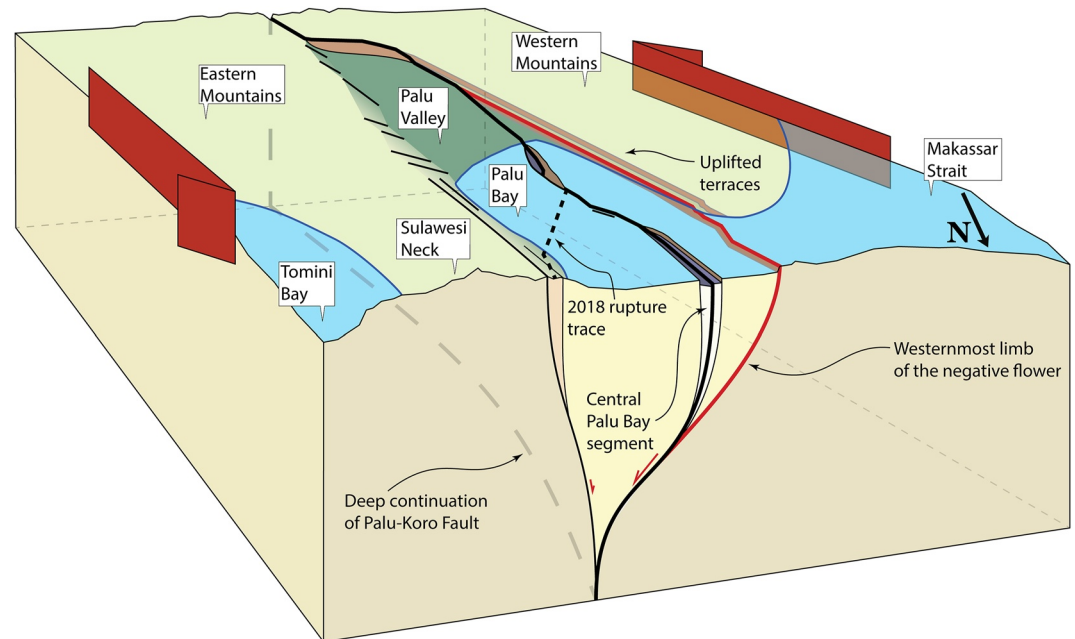


Figure 5. Synoptic view of the transensional setting (i.e., a combination of strike-slip and normal faulting) of the Palu-Koro fault in the Palu Valley and Palu Bay region, using the active fault trace from the 2018 rupture and other features in the structural geology (Bellier et al., 1998, 2006; Hennig et al., 2017; Jaya et al., 2019; Leeuwen & Muhandjo, 2005; Natawidjaja et al., 2020; Watkinson & Hall, 2017). In our interpretation, the Palu Valley and Bay region is the downthrown part of a negative flower structure; the westernmost limb runs along the west side of Palu Valley and Bay (red line) with many offset terraces, streams and cut alluvial fans and the largest normal motion (Bellier et al., 1998, 2001, 2006; Patria & Putra, 2020; Watkinson & Hall, 2017). The eastern side of Palu Valley and Bay displays more distributed differential motion, with multiple discontinuous fault strands (Natawidjaja et al., 2020; Watkinson & Hall, 2017). The Central Palu Bay segment (Natawidjaja et al., 2020) appears relevant for the 2018 rupture trace only up to the point where the rupture changes strike abruptly toward the Sulawesi Neck, shown here with a dotted black line (see also Figure 3). Below the bay, we expect a fault bend that connects the parallel fault strands north and south of the bay. Being a right stepping fault segment on a left-lateral strike-slip fault, we foresee transpressional deformation (i.e., a combination of strike-slip and thrust faulting) on this restraining fault bend. In our interpretation, the main fault at depth has a strike of $\sim 350^\circ$, up to the point where it leaves Palu Valley in the south, from where it changes strike southward. The vertical offsets have been exaggerated for visual purposes.

et al., 2002). Hence, we interpret surface faults as being consistent with Riedel shear orientations (upper left panel of Figure 4), linked to an underlying fault. We take the strikes of the fault structures traced from the 2018 fault rupture and other features in the structural geology of the Palu-Koro fault region between $0.12N$ and $-1.27S$ (Bellier et al., 1998; Leeuwen & Muhandjo, 2005; Natawidjaja et al., 2020; Watkinson & Hall, 2017). In the lower panels of Figure 4 we compare these fault strikes with the subsidiary fault orientations of a Riedel shear system (Tchalenko, 1970) considering two scenarios: a main fault striking $\sim 350^\circ$, and a main fault that strikes parallel to the previously hypothesized main fault that bounds the west side of Palu Valley and Bay at $\sim 340^\circ$ (e.g., Bellier et al., 2001, 2006; Natawidjaja et al., 2020; Walpersdorf, Vigny, et al., 1998). Both these options fall within the observed maximum horizontal stress directions (Heidbach et al., 2018). Only a main fault striking at 350° leads to a Riedel shear system that is in agreement with the observed fault distribution in the deformation zone of the Palu-Koro fault, leading to a distinctly more northward rather than NNW orientation. As a consequence, the west side of Palu Valley and Bay would be a Riedel shear (R) and the outer limb of the negative flower, illustrated by Figure 5. In our interpretation, the deep continuation of the Palu-Koro fault strikes away from the west side of the Palu Valley and Bay, and runs beneath the Sulawesi Neck instead, just east of Palu Bay. A deep continuation of the Palu-Koro fault just onshore the eastern side of Palu Bay is also supported by pre-2018 inter-seismic displacements across the fault, as observed by the GPS transect of Socquet et al. (2006). The location of the steepest gradient in fault parallel GPS velocities indicates that the deep fault lies west of Palu Bay. Their fault model includes locking down to 12 km depth, and has a strike parallel to the previously discussed hypothesis of a main fault at the west side of the Bay, similar as Stevens et al. (1999). However, as GPS vector azimuths in Socquet

et al. (2006) show a consistent clockwise misfit of 5–15°, we suggest that a ~350° strike of the deep continuation of the Palu-Koro fault may solve these azimuthal misfits.

3.3. Fault Bends in a Transtensional Basin Structure

The 2018 rupture started above the hypothesized deep segment below the Sulawesi Neck, and only south of Palu Bay it follows the western faults of the Palu-Koro fault system. We note that a structural interpretation of the Palu Valley and Bay (and further offshore) domain as a pull-apart basin (Natawidjaja et al., 2020) does not fit this geodetic observation, as this would require a northward continuation of the main, deep fault west of the Bay. Furthermore, a pull-apart basin does not match the subsidiary Riedel shear fault orientations well (lower right panel of Figure 4). Using a deep fault orientation of 350°, we find matching orientations between normal faults (T) in the Riedel shear system and releasing bends at the southern entrance of Palu Valley and within Palu Bay, along the eastern side of Palu Valley and just offshore Balaesang Peninsula (Natawidjaja et al., 2020). The hypocenter distribution beneath and offshore the Sulawesi Neck (Supendi et al., 2020) agrees with our structural interpretation of the transtensional basin system with (potential) activity on multiple fault strands (especially before the 2018 event). The post-earthquake seismicity does seem to show a preference to the Sulawesi Neck, surrounding our inferred main fault at depth. The surface displacements indicate a strike change between the rupture in the Sulawesi Neck and Palu Valley. Thus, the potential fault bend across Palu Bay would be a right-stepping, restraining bend within the left-lateral Palu fault system, resulting in a transpressional structure, in an overall transtensional setting. The restraining bend will then form a paired bend together with the releasing bend in southern Palu Valley, a feature that has been found more often along strike-slip faults (Mann, 2007).

The tectonic setting of strike-slip faults does not commonly lead to tsunamigenic earthquakes, due to the predominance of co-seismic surface motions in the horizontal plane. The transtensional nature of the Palu-Koro fault, with multiple fault segments at shallow levels, indicates the possibility for dip-slip components that enhance vertical surface displacements during earthquakes. The Palu-Koro fault thus hosts potential for localized vertical sub-marine motions able to generate tsunamis (similar to the cases described by Geist and Zoback, 1999; Tinti et al., 2006).

4. Fault Slip and Tsunami Modeling

4.1. Fault Model and Inversion

We invert the observed surface displacements to constrain the co-seismic fault slip distribution. For the onshore part, the fault trace is clearly visible, as shown by Figure 3, especially in Palu Valley (a similar inference has been made from optical data (Sotiris et al., 2018)), and that allows us to clearly define successive fault segments. Because we do not have direct observations of the course of the ruptured fault below the bay we consider multiple scenarios for fault geometries there. Modeling suggest that the presence of a fault bend that links the northern and southern segments increases the ability for the rupture to propagate (Oglesby, 2005). The displacement field at the location where the fault enters the bay suggests a strike change in the direction of the southern part of the fault (Figure 3), which is in favor of a continuous rupture from north to south. Furthermore, the analysis by Biasi and Wesnousky (2016) of mapped surface ruptures indicates that an earthquake passing a >5 km step-over, as would result from a discontinuity between the northern and southern fault strands, is relatively rare for strike-slip. Nevertheless, we also test a scenario where we treat the rupture as discontinuous (e.g., Williamson et al., 2020). In all cases, we are looking for a minimum-complexity fault model with a single fault strand, as the seismological moment tensor is a dominantly (90%) double couple (USGS, 2018). We treat the orientation of the connecting fault segments below the bay as a free parameter. Because we lack a priori information about the dip orientation of the ruptured fault, we solve for the dip angle of each segment in the inversion. As the fault likely has a negative flower structure (see Figure 5 for a schematic representation), the dip angle is likely to change with depth. For the cross-basin deep fault (Watkinson & Hall, 2017) we assume a single deep fault that underlies the shallow fault segments, with an approximate 350° strike (see Section 3). Two areas, distinct from the main strike-slip rupture, show notable subsidence and horizontal displacement perpendicular to the main fault that we interpret as slip on normal faults: east of the main fault in the Sulawesi Neck (point g in Figure 3) and northwest of the main fault in the Balaesang peninsula (as also proposed by Socquet et al. (2019)).

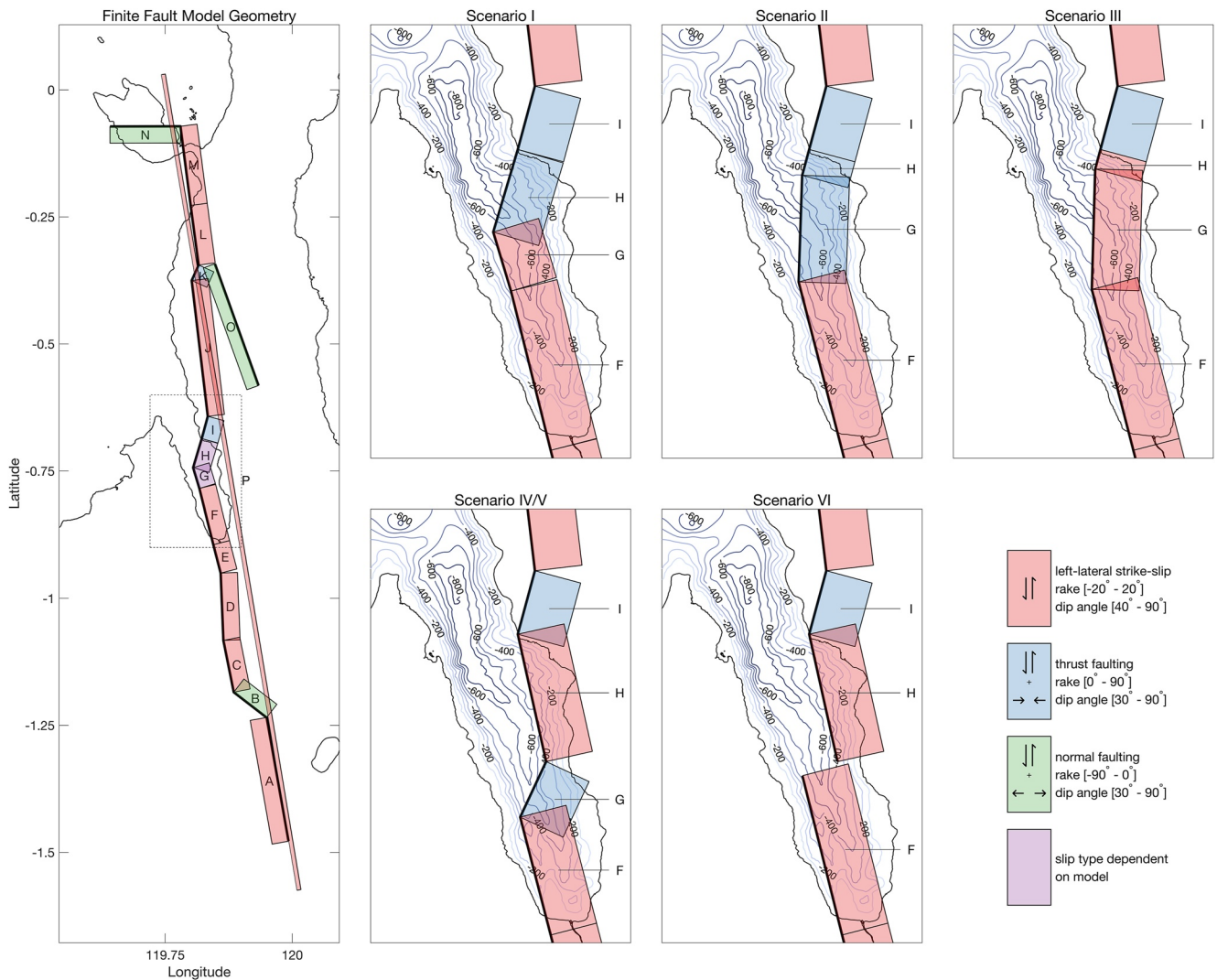


Figure 6. Fault model surface trace geometry. (Left panel) Fault discretization in segments and slip constraints. The rectangle depicts the bay section. (Right panel) Six model scenarios for the bay section of the rupture. Thick black line represents the segmentation of the fault trace. The shallow curved segments in Figure 5 (red line) are represented in the model by planes with a dip angle that is consistent with the updip part of the flower structure, as this dip angle has the largest imprint on the surface displacements. Shallow segments A to O span depths between 0 and 7 km. The deep cross-basin fault P ranges between 7 and 22 km depth. Background: model bathymetry.

4.1.1. Fault Segmentation and Discretization

We use 16 fault segments to characterize the fault geometry; 13 segments belong to the main fault: A to M from the south to north, including four fault bend segments (B, H, I, and K) that differ in strike from the dominant north-south strike (left panel of Figure 6). Segments F, G, and H comprise the connection through Palu Bay, where F and H are partly onshore so that their strike angles are fixed based on the visible fault trace. Segment O represents the normal fault parallel to the main rupture; the fault in the Belaesang peninsula we model by segment N; the deep cross-basin fault by segment P. We subdivide the shallow segments (0–7 km depth) in multiple patches that increase in size with depth to impose increasing smoothness with depth; the cross-basin fault ranges from 7 to 22 km depth (see Section S5 in Supporting Information S1 for more details).

4.1.2. Slip Inversion

We apply a Bayesian approach that samples the posterior probability density function (PDF) of each model parameter through a Markov chain Monte Carlo (MCMC) scheme, incorporating an automatic step size selection (Bagnardi & Hooper, 2018). In the inversion we use the original GPS displacements (and estimated uncertainties)

and downsampled (In)SAR displacement fields. For the latter we estimate the spatial error covariance, see the Supporting Information S1. We use rectangular dislocation sources in an elastic half-space (Okada, 1985) with a Poisson's ratio of $\nu = 0.25$ and a shear modulus of 32 GPa. We solve for slip magnitude, in a 0–10 m range, and rake per patch, for which constraints are needed to avoid alternating slip directions from patch to patch. For the strike-slip segments we constrain the rake to be in the -20° to 20° range as we expect the rupture to be dominated by the left-lateral strike-slip. Right-stepping fault bends (H, I, K) have rake constraints of 0° – 90° (i.e., thrusting with a left-lateral component), while the left-stepping fault bends (B, N) and the parallel normal fault (O) have a -90° to 0° rake constraint (normal faulting with a left-lateral component), to reflect the expected compression and extension, respectively, for a left-lateral fault system.

We solve for the dip angle of each segment. The asymmetry of the displacements suggests east dipping faults, except for the most southerly segment A (Figure 3). The allowed dip angle for strike-slip segments is in the range (40° – 90°) and (30° – 90°) for the remaining segments. Segments F and H are continuations of onshore segments (E and I, respectively) and we solve for their endpoints below the bay; the length and orientation of segment G are thus (free) parameters, as this segment is entirely located offshore.

As the slip magnitudes of the deep patches are usually poorly constrained by the surface observations, changes in the slip magnitudes of the deep patches may not cause a large change to the posterior probability. Therefore, we apply a prior constraint on the seismic moment, assuming a Gaussian distribution with the mean from the USGS solution ($2.497 \cdot 10^{20}$ N·m⁻¹) and a 10% standard deviation. Simultaneously we estimate a bilinear plane for each SAR-derived displacement field to approximate residual long wavelength errors due to atmosphere, tides, orbit errors and plate motions. The inversion result consists of posterior PDFs for all estimated parameters, based on a large set of tested fault slip solutions (~5 million), with a varying fit to the data.

4.1.3. Fault Orientation Below the Bay: Six Model Scenarios

Because there is no data that precisely locates the course of the rupture below the bay, we test different scenarios, shown in Figure 6, which only differ with respect to the bay segments (i.e., F, G, and H). Here, we vary the slip constraints and/or fault orientation between four different tectonically feasible scenarios. The shallow rupture below the bay may include left-lateral strike-slip faults as a continuation of the onshore faults, as well as a right-stepping fault bend to connect the parallel segments north and south of the bay. In this context the fault bend would become a restraining bend, leading to a combination of left-lateral strike-slip and thrusting (i.e., transpression). In *Scenario I* we consider segment H to be the complete fault bend, implying dominant thrusting; segments F and G are forced to be strike-slip segments. Alternatively, to allow for a gradual strike change of the fault bend, in *Scenario II* we consider both H and G to be fault bends, and only F is considered strike-slip. *Scenario III* explores the possibility that all bay segments are dominantly strike-slip. Next, as some studies advocated for a tsunami source relatively far south in the Bay, based on tsunami arrival times at the Pantoloan tide gauge (Carvajal et al., 2019), we force the location of significant uplift, that is, the fault bend, to be in the southern part of the Bay in *Scenario IV*. To do so, we set the middle segment G as the fault bend, while we set the northern and southern segments F and H as strike-slip in *Scenario IV*. We fix the length of the northern bay segment H at 10 km, such that the fault bend G situates at the 170 s travel time contour from Carvajal et al. (2019). *Scenario V* is a variation on the former, where the southern segment F has a free strike. As a last model we investigate a possible discontinuity in the rupture propagation, with no slip on the middle bay segment, resulting in a step-over between the two parallel fault segments H and F in *Scenario VI* (a setup previously explored by Williamson et al. (2020)). To suppress possible vertical motions within the 170 s travel time contour with respect to Pantoloan, we add quasi-observations of zero vertical displacement (with a standard deviation of 1 mm) above segment H in scenarios IV, V, and VI.

4.1.4. Model Initialization

To cover a broad search space for the fault parameters that we aim to estimate, especially the fault geometry below the bay, we apply simulated annealing in the first steps of our inversion. We apply the simulated annealing approach (Van Laarhoven & Aarts, 1987) to scenarios I, IV, V, and VI to test model parameters in a large search space. We then use the optimal solutions inverted from the simulated annealing as the initial solutions of the later Bayesian inversion for scenarios I, IV, V, and VI, whereas the initial solutions of model scenarios II and III are adapted from the optimal maximum posterior (MAP) solution of the Bayesian inversion of scenario I.

5. Tsunami Modeling and Bathymetry

For the numerical simulation of the tsunami propagation and inundation we make use of a fully-nonlinear and non-hydrostatic, barotropic model, H2Ocean (Cui et al., 2010, 2012). The model is based on the nonlinear shallow water equations discretized using an unstructured finite volume approach. H2Ocean preserves mass and momentum in local cells as well as maintaining the positivity of the water depth in the case of wetting and drying. Model outcomes have been validated against a number of classical test cases, among others wave propagation over a submerged bar, the Okushiri Island Tsunami laboratory experiment and the Berkhoff Shoal test case (Cui et al., 2012, 2014). Furthermore, the model was successfully used to simulate the evolution and maximum run-up and inundation height of the 2004 Indian Ocean Tsunami and 2011 Tohoku Tsunami (Cui et al., 2010; Hooper et al., 2013; Shimozono et al., 2014).

The combined digital terrain model (DTM)/Bathymetry grid for the tsunami modeling has an 8 m DTM resolution and ≈ 185 m bathymetry resolution, and is based on data provided by BIG (Badan Informasi Geospasial, Indonesia). We have calibrated both DTM and bathymetry to mean sea level (see Section S7 in Supporting Information S1). The reported root mean square error of the DTM is 2.79 m. We use a computational mesh, generated using OceanMesh2D (Roberts et al., 2019), with a 5–10 m resolution for the inundated area inside Palu Bay and the adjacent coastal area. We adapt the grid resolution gradually: from 250 m close to the epicenter to 2.5 km in the Makassar basin west of Sulawesi.

The tsunami model is driven by instantaneous vertical displacements of the sea surface and bed. The effective vertical displacement is calculated following Tanioka and Satake (1996):

$$d = -u_x \frac{\partial H}{\partial x} - u_y \frac{\partial H}{\partial y} + u_z \quad (1)$$

where u_x , u_y , and u_z are the displacement components in east, north and up directions from the co-seismic slip model, respectively, and H is the bathymetry (defined here positive upward, hence the minus signs). Since the earthquake occurred close to the time of the high tide, the tidal elevation may contribute significantly to the tsunami inundation. Therefore, we set the initial still water level to 0.85 m, the tidal elevation level observed at the Pantoloan tide gauge just before the earthquake. We use a quadratic friction law with a Chezy coefficient of 0.003. The timesteps are variable and are determined by setting the Courant number to 0.8 (Cui et al., 2010).

We compare modeled tsunami elevations η with video waveforms derived by Carvajal et al. (2019), by computing the relative tsunami elevation, that takes into account the vertical displacement of a point of observation:

$$\eta_{\text{rel}} = \eta - u_z \quad (2)$$

whereas for computing inundation we update the bathymetry by d , the spatial vertical displacement. To compute inundation distance and runup height along the coastline (taken as the zero contour from the combined DTM/bathymetry) we use the following procedure. For each inundated grid point on land we find the nearest point on the coastline (projection of the inundated grid point onto the coastline) and calculate the distance between the two. Next we divide the coastline into short segments (~ 10 m). We then compare inundation heights and distances to the coastline of the grid points projected into the same segment. Per segment, we take the largest distance as the inundation distance and the maximum inundation height as the runup height.

5.1. Tsunami Model Sensitivity to Slip Uncertainties

Because tsunami models are computationally expensive, we do not run all models that underly the slip inversion, instead we focus on the optimally fitting model for each scenario. Still, we want to be able to test how uncertainties in the slip solutions affect tsunami model results, and hence how robust our tsunami model results are for each of the fault scenarios. Therefore, for each scenario we draw a number of less likely models from the large distribution of fault slip solutions. We run the tsunami model for a selection of less likely models, which we select based on (a) deviations with respect to the mean vertically displaced water volume, or (b) differences compared to the mean vertical displacement field.

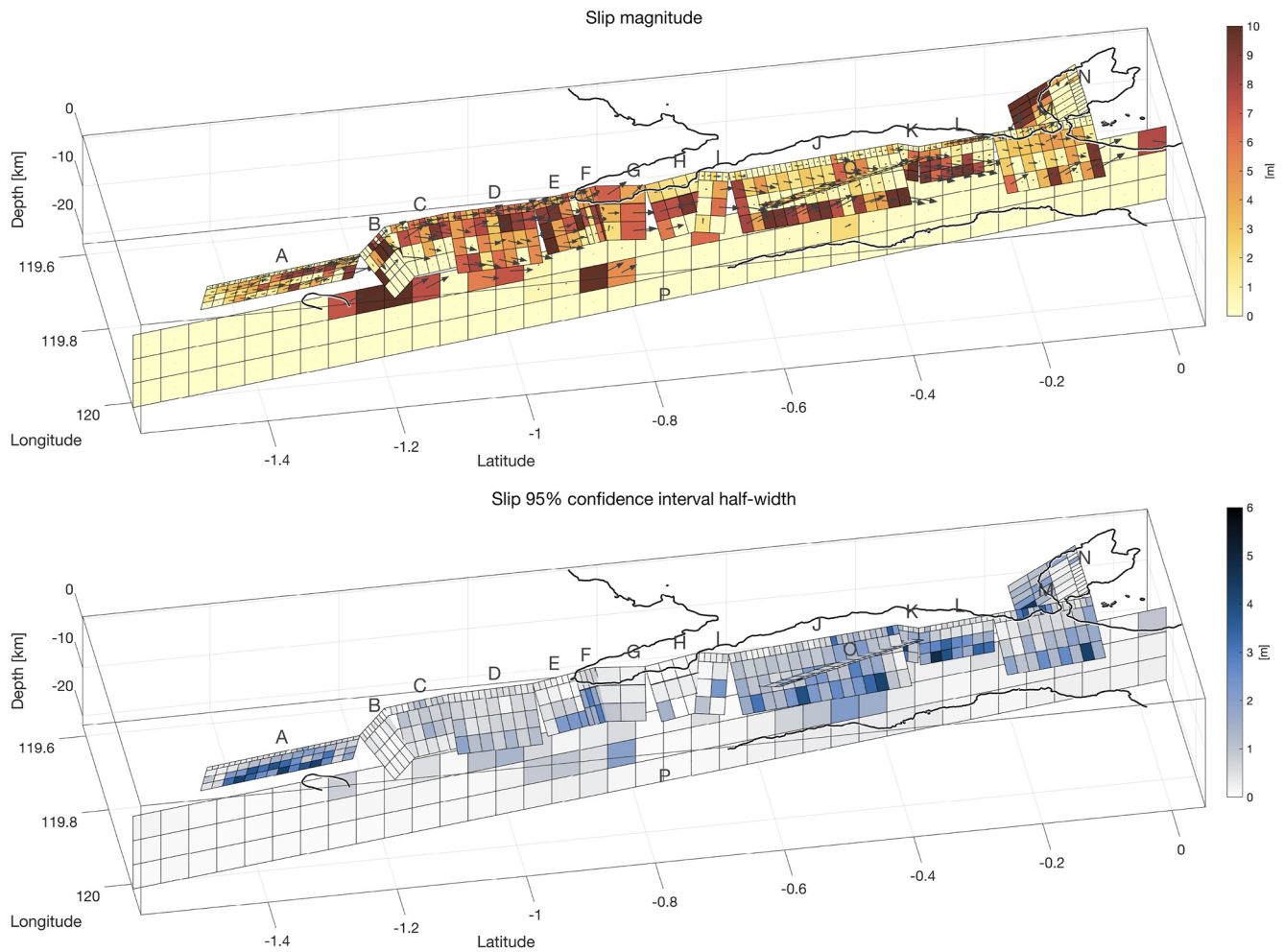


Figure 7. Estimated median fault slip distribution (Scenario IV). (top) Slip magnitude, with arrows indicating slip direction. (bottom) Uncertainties of the slip magnitude, shown as the half-width of the 95% confidence interval, estimated from the slip probability distributions. Bay segments are F, G, and H.

5.2. Tsunami Inundation Distance From Satellite Imagery

We derive tsunami inundation by classifying pre-post tsunami satellite imagery from the Planet (1 October 2018) and Worldview-3 (4 November 2017; 20 February 2018; 17 August 2018; 1 October 2018; 2 October 2018) archives. For this purpose, we visually compare the pre- and post-tsunami satellite images to manually detect changes that indicate tsunami impact (e.g., coastline changes, debris cover, etc.) and digitize the outlines of inundated areas based on this comparison. We take the minimum distance from the inundation outline to the coast to derive the inundation distance. For survey data, we use the reported locations from runup height and inundation height observations (Goda et al., 2019; Mikami et al., 2019; Omira et al., 2019; Putra et al., 2019; Syamsidik et al., 2019; Widiyanto et al., 2019) and project these on the coastline to compute inundation distances that are consistent with the other calculated inundation distances.

6. Finite Fault Slip Estimate

6.1. General Fault and Slip Characteristics

The Bayesian slip inversion results in a probability distribution for the estimated fault geometry and slip parameters. Figure 7 shows our median estimate for the fault slip distribution (*Scenario IV*, but results for the different scenarios only differ in the Bay area), demonstrating a dominance of shallow strike-slip, mostly limited to the upper 10 km. On the segments south of the bay, large slip (>5 m) continues up to the surface, whereas segments north of the bay feature no or minor slip on the upper segments, implying that the rupture does not reach the

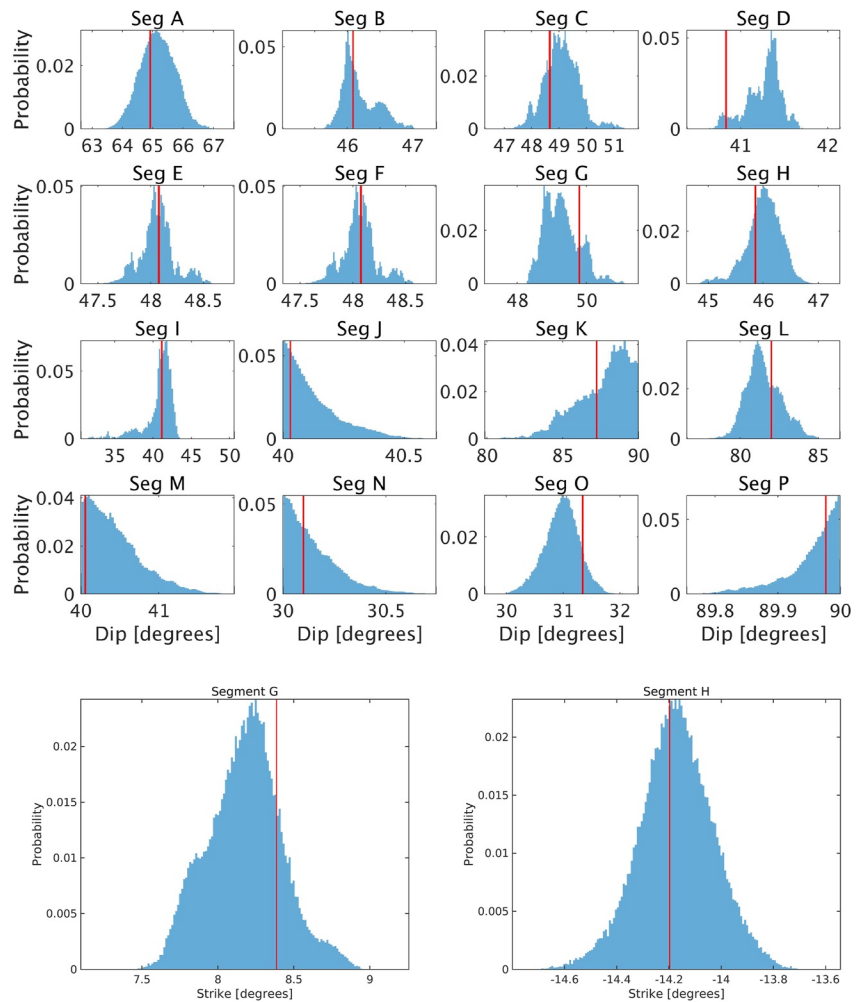


Figure 8. Posterior probability density functions (for *Scenario IV*) of: (top panels) the estimated segment dip angles. All segments dip toward the east, except A and O dip toward the west, and N dips toward the south. (lower row) The strike angles of the central (G) and northern (H) bay segments with a free strike. Red lines denote the value for the maximum posterior (optimal) solution. For locations of the segments, see Figure 7.

surface there. On the north-south striking segments strike-slip is dominant, but we find significant dip-slip at the fault bend segments. Specifically, we estimate a large normal component (>1 m) on the releasing fault bend segment B, in southern Palu Valley, clearly connected to the large subsidence observed by GPS and SAR, see Figure 3. Furthermore, we find significant dip-slip on the segments below the bay (where we expect a restraining bend), for all tested scenarios. We estimate uncertainties for inverted slip by taking the half-width of the 95% confidence interval of the slip PDFs (of which we show a selection in Figures S9–S11 in Supporting Information S1). Uncertainties in strike-slip and dip-slip components are small in the Palu Valley area, where we have many observations close to the surface rupture. On some other segments the slip is less well constrained; notably on the normal fault segment below the Sulawesi Neck (O), below the Bay (segments F, G, H) and the deeper parts of the Sulawesi Neck segments K and L. Especially on the deeper parts of the normal fault (O), and the deeper part of the southernmost segment the 2σ uncertainties are on the order of the resolved slip. We find short wavelength variability of slip; on the aforementioned segments with high slip uncertainties, we attribute this to the absence of smoothing constraints in the inversion. On the shallow segments though—where uncertainties are generally low—the fluctuation of slip is likely real, as it reflects the spatial variability of co-seismic surface displacement along the fault (see Figure 3).

The estimated dip angles show a preference for 40° – 50° , except below the peninsula (segments K and L) and the deep segment P, see Figure 8. Normal faulting on the parallel segment O reflects the observed subsidence and

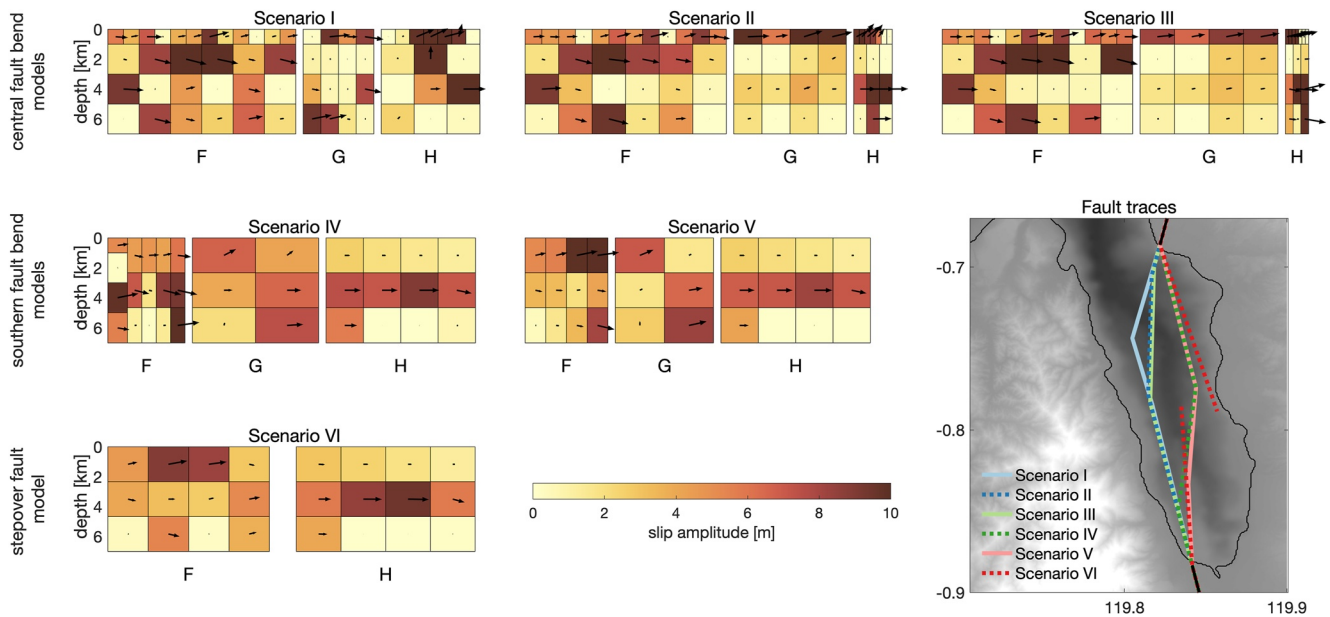


Figure 9. Focus on the inverted slip (MAP) on the fault below Palu Bay for the various fault scenarios. Bay fault segments F, G, and H (from south to north) have different rake boundary conditions between the scenarios, see Figure 6. The scenarios are grouped as *I, II, III* having a central fault bend, focusing dip-slip in the north (segments G and H); scenarios *IV, V* incorporating a southern fault bend, that allows dip-slip more southerly (segment G), whereas scenario *V* features a step-over (missing segment G). The map shows the various estimated fault traces.

eastward motions. All scenarios give similar fits to the geodetic data, Figure S13 in Supporting Information S1 shows the fits to the SAR displacements fields. The displacements resulting from the median slip distribution well reproduce the GPS displacements, with no significant differences between the scenarios in the Bay area.

6.2. Inverted Slip Below the Bay

All scenarios provide a similar fit to the surface displacements. All scenarios feature significant strike-slip below the bay. Moreover, Figure 9 shows that to explain the GPS displacements around the bay, all scenarios require substantial thrusting below the bay. GPS vectors south of the bay (Figure 3) point toward the fault, rather than parallel to the mean strike of the fault. We can only explain the azimuth of the GPS displacements by thrusting (dip-slip) on shallow sections of the bay segments of the fault (see Figure S12 in Supporting Information S1). In scenarios *I, II* and *IV, V*, we have designated segments as oblique thrust. Those thrust segments become bends in the inversion, by having a strike deviating from the average fault strike. These bay segments also take up the largest part of the thrust slip (even though thrusting is allowed on the left-lateral strike segments), especially in the most shallow parts. In *Scenario III* and *Scenario VI*, where we have not enforced slip to be oblique thrusting on any of the segments, thrusting occurs as well below the bay in those scenarios, but it is more distributed and its magnitude is smaller. In *Scenario III* (no explicit thrust segment) the inversion results in thrusting on all bay segments, in *Scenario VI* (step-over model) thrusting occurs mainly on the shallow parts of the southern F segment. In *Scenario VI*, the inversion prefers a strike of the most southern bay segment (F) that does not follow the western coast of the bay (such as in Figure 1), but rather strikes to the NNE, likely in order to fit the azimuth of the co-seismic GPS vectors south of the bay. A result with two sub-parallel fault branches and a step-over with considerable overlap between the northern and southern segments (H and F, respectively), where the southern segment follows the western bay coast does not fit well with the geodetic data. Already within the initial step of the inversion of *Scenario VI*, the simulated annealing phase, overlap of segments F and H is tested, but subsequently discarded because of large misfits with the data. The estimated strikes, of those segments that are allowed to change during the inversion, have uncertainties on the order of a few degrees, see Figure 8 for PDFs.

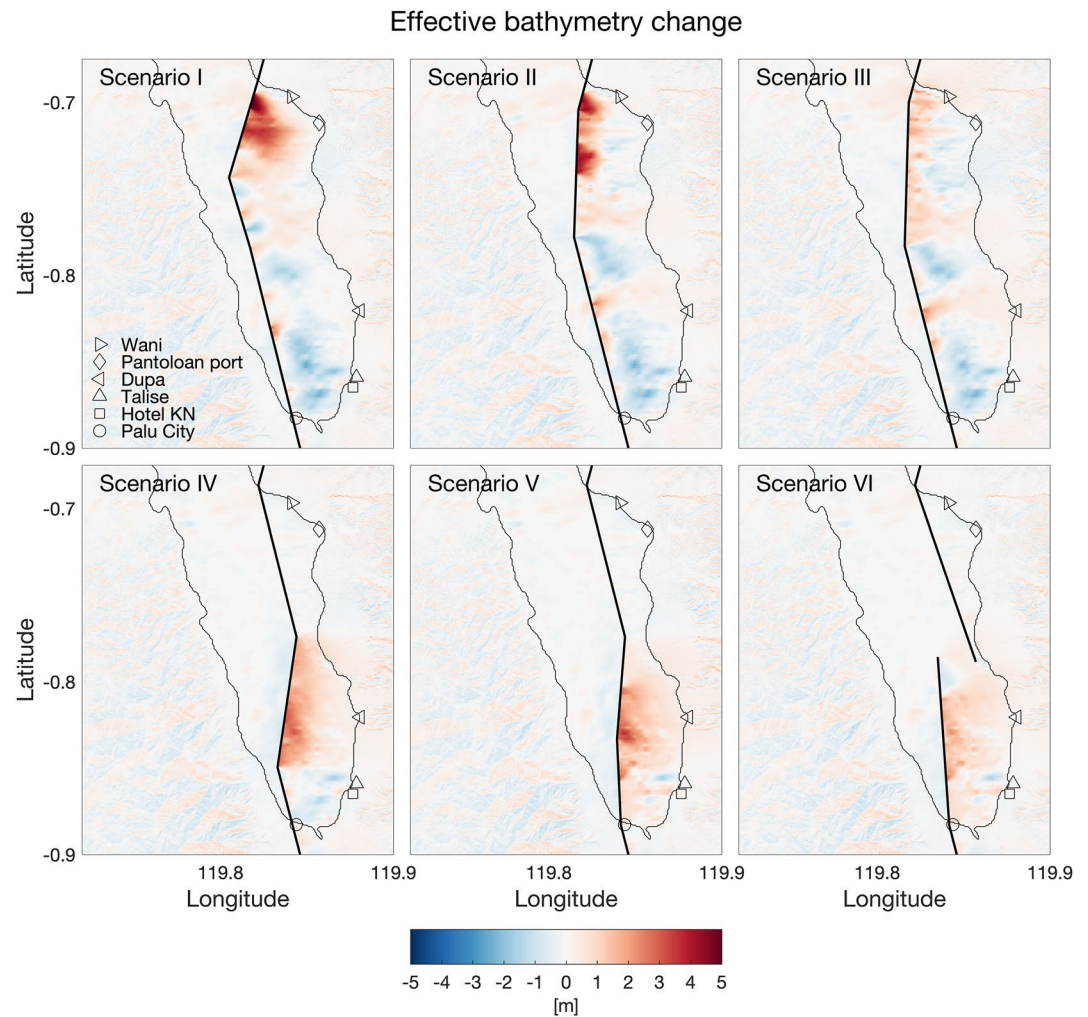


Figure 10. Effective vertical displacements d (Equation 1) below Palu Bay due to co-seismic vertical and horizontal displacements, based on the maximum posterior (MAP) of the six fault scenarios. The black line represents the fault trace. Also shown are the six sites for which Carvajal et al. (2019) assembled tsunami elevation waveforms, and that we use in the subsequent section to test the fault scenarios.

6.3. Co-seismic Bathymetry Changes Below the Bay

As dip-slip has the most influence on vertical co-seismic displacements, the thrust patterns have a direct effect on vertical displacements below the bay, implying uplift above the thrusting patches. Figure 10 depicts the modeled effective bathymetry change d for all scenarios. Major regions of effective uplift result from thrusting on faults, whereas distributed subsidence occurs above the down-dip end of the thrust slip. The modeled effective bathymetry change d (Figure 10) combines the direct vertical displacements and the effect of horizontal displacement on steep slopes (Equation 1). Figure S15 in Supporting Information S1 shows the separated contributions from vertical and horizontal co-seismic displacements to the effective bathymetry change. Uplift in scenarios *I*, *II*, *III* focuses in the north of the bay, with smaller patches of uplift along the southern F segment. The magnitude of uplift is larger for scenarios where we constrain the segments to be (oblique) thrusting (scenarios *I*, *II*), with peak values around 5 m. In *Scenario IV* and *V* the uplifted area shifts to the south, above the central fault bend represented by segment G, while peak uplift values are roughly half as those of scenarios *I*, *II*. The absence of a fault bend in *Scenario VI* leads to smaller uplift values compared to scenarios with a fault bend. The contributions from horizontal displacements of the sloped bathymetry are generally second order effects. Scenarios *I*, *II*, *III* predict broad regions of subsidence in the southern part of bay, while subsiding areas in scenarios *IV*, *V*, *VI* are smaller. This subsidence is largely canceled by the effect of horizontal displacements (see Figure S15 in

Supporting Information S1), as the combination of a sloped bay floor and a northward displacement east of the fault effectively increases the bathymetry depth.

7. Tsunami Model Results and Observational Constraints

7.1. Tsunami Arrival for Six Fault Scenarios

Before examining the details of the modeled tsunami evolution, we compare the tsunami waveforms of each scenario to the available tsunami timing observations. We focus primarily on the arrival times of the leading waves of elevation (positive) or depression (negative). We typically neglected reflected waves as it is not possible to determine the source region due to the resulting interference. Subsidence is associated with negative polarity of the leading wave, while uplift is associated with positive polarity. The arrival time, amplitude and polarity of the tsunami waves at the coast provide a first order check of the likeliness of the co-seismic uplift patterns and location. However, the observational constraints on the tsunami evolution are quite sparse. The most reliable sources of information are the waveforms at six locations along the southern and eastern bay coast that Carvajal et al. (2019) derived on the basis of tsunami videos made during and directly after the earthquake. The only tide gauge in the bay, at the harbor of Pantoloan, is likely of little use to observe the tsunami arrival; as data at the tide gauge has been averaged over 30 s and output at a 1 min sampling (Sepúlveda et al., 2020), it cannot be used to describe the short period waves that have been observed from the videos. As our inversion is independent of tsunami timing data, our predictions are unlikely to fit the video tsunami waveforms exactly. Rather we judge the models for a qualitative agreement with the available data.

Figure 11 shows the model evolution of the relative tsunami elevation (Equation 2) for the first 6 min after the earthquake, compared to the video waveforms deduced by Carvajal et al. (2019).

7.1.1. Northeastern Sites: Pantoloan and Wani

At Pantoloan the largest, and presumably first, waves have been relatively well observed by the motion of a ship in the dock by a camera. The video waveform shows a first major, negative wave at around 3 min since the start of ground shaking, followed by a 2.5 m wave of elevation less than 30 s later. We observe that all scenarios with a northern fault bend, scenarios *I*, *II*, *III*, lead to an arrival of a major positive wave between 1 and 2 min, well before the first observed wave. Scenario *III* leads to reduced amplitudes of the first waves compared to Scenario *I* and *II*. For Wani, similar as for Pantoloan, scenarios *I*, *II*, *III* predict an early wave arrival (1 min) before the onset of flooding as observed. Scenarios with a southern fault bend *IV*, *V*, *VI* produce a first, positive wave arriving 3 min, but underestimate the wave amplitude by approximately a factor of two.

7.1.2. Southeastern Sites: Dupa, Talise and Hotel KN

The video waveforms for Talise and Hotel KN are based on videos that record the earthquake induced shaking, and have thus a reliable timing. For Talise it is merely the drawdown of water that is captured on the video, within a minute from the start of the shaking. We model a fast (<1 min) approach of a wave of depression near Talise and Hotel KN (see the Supplemental Videos, <https://surfdrive.surf.nl/files/index.php/s/QKKsMSG0SOLQUGy/download>). For scenarios *I*, *II*, *III* the wave of depression has the largest amplitude, while in scenarios *V*, *VI* this negative wave just misses Talise due to interference with a wave of elevation. The subsequent inundation by waves of elevation is not visible from the Talise video, but it is recorded from cameras at Hotel KN, just south of Talise. All scenarios predict a negative wave at approximately 1 min for Hotel KN (the videos at this location do not provide information on the first 1:40 min; Carvajal et al., 2019), quickly followed by the arrival of a positive wave. Scenarios *IV*, *V*, *VI* predict this arrival 20 s earlier than the video waveform, scenarios *I*, *II*, *III* lead to a 20 s later arrival compared to the video waveform. Amplitudes between video waveform and models are very similar.

At Dupa, north of the two former locations, the earthquake itself is not recorded by camera, resulting in a time bias. In the video it takes 1:50 before the arrival of the positive wave (Carvajal et al., 2019), while a tsunami bore can be seen close to the coast 30 s prior to arrival. Assuming that the duration of the strongest earthquake shaking is about 30 s (as is visible in the video from nearby Talise), the arrival of the positive wave can be at the earliest at 2:20 since the start of the earthquake, which is 30 s earlier than suggested by Carvajal et al. (2019). Scenarios *I*, *II*, *III* all feature a first negative wave, and small (<1 m) positive waves after 2:30 min. Scenarios *IV*, *V*, *VI* do not lead to initial negative waves (due to absence of subsidence near Dupa), and predict the first major positive waves at 1:50 min.

Comparison waveforms for different fault scenarios

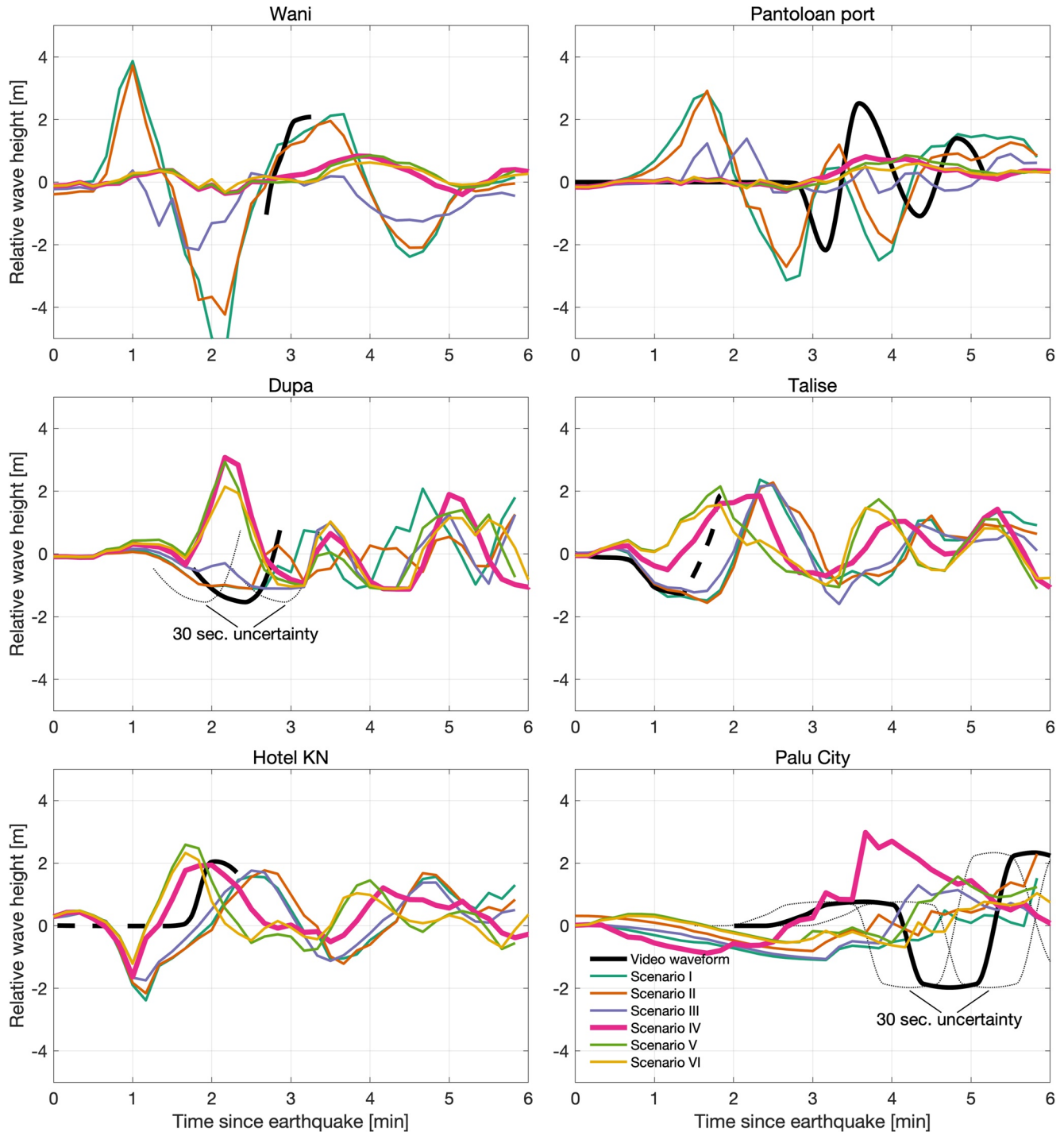


Figure 11. Approximate tsunami height at six locations for which tsunami observations are available, based on video analysis from Carvajal et al. (2019), and model predictions for tsunami height. For locations see Figure 10. Time series for Dupa and Palu City have a bias in timing as the start of the videos does not include the earthquake (Sepúlveda et al., 2020). *Scenario IV* represents our preferred solution. A dashed line represents a lower confidence estimate (Carvajal et al., 2019).

7.1.3. Palu City

Whereas the nearby locations Hotel KN and Talise have very early arrival times of the first positive waves, Carvajal et al. (2019) suggest that the first, and positive, wave arrives at Palu after 3 min, while there is a time bias, as all videos from Palu start after the earthquake. Sepúlveda et al. (2020) suggest that for Palu City the time bias uncertainty is 30 s. Even though the rupture went through Palu City, waves are likely to arrive relatively late due to the shallow bathymetry offshore Palu. All scenarios predict an initial drawdown of water at the Palu coast (<1 m), and positive waves arriving after 3 min. In *Scenario IV*, the timing of the first wave arrival at about 3 minutes corresponds to the video waveform, while the other scenarios predict a first arrival after 4–5 min. Except for *Scenario VI*, the crest amplitude is comparable to that of the video waveform, yet none of the models reproduce the negative wave that follows the first positive wave around 4–5 min after the earthquake.

7.2. Preferred Fault Scenario: Southern Located Fault Bend

In selecting a scenario that best explains the observed tsunami waveforms, we prefer scenarios that best explain arrival time and initial polarity and amplitude, while we disqualify scenarios that include significant initial waves that did not occur according to the available observations. As all our model scenarios with a northern fault bend (scenarios *I, II, III*) lead to a tsunami arrival that is too early in northeastern sites Pantoloan and Wani, we discard these scenarios. In scenarios *IV, V, VI* the areas of major uplift localize in the south, which avoids a tsunami that arrives too early in Pantoloan and Wani. As *Scenario VI* underestimates the wave amplitude in Palu City, because it lacks a fault bend, we discard this scenario also. We choose *Scenario IV* as a preferred fault scenario, since it explains wave amplitudes and polarity for the other sites (Dupa, Talise, Hotel KN, and Palu City) and does a relatively good job in predicting the timing of the first arrivals, even though this scenario lacks significant waves in the northeast. *Scenario V* is comparable to *Scenario IV*, but as the latter has a more prominent southern corner at the fault bend (Figure 10) it has more pronounced waves traveling directly toward Palu, which improves the arrival time fit. In the remainder of the paper we show results for scenario *IV*, and include the other scenarios in the Section S8 in Supporting Information S1.

7.2.1. Spatiotemporal Evolution of the Initial Tsunami Waves

Our preferred scenario *IV* predicts the propagation of two approximate north-south wave fronts in the direction of both the western and eastern bay coastlines, see Figure 12. At 1:40 after the earthquake, the model predicts reflections at the western coast that take the form of localized elevation perturbations (between latitudes -0.85 and -0.8), which result in subsequent ringing (see Movie S1 in Supporting Information S1). At the east coast the positive polarity waves arrive shortly after 1:40. The panels show also the relatively slow approach of several tsunami fronts toward western Palu, which approach Palu from different directions (3:20 and 4:10) due to the local shallow bathymetry. In this scenario the waves radiating toward the north have only moderate amplitudes compared to the waves traveling in the N-E and southern directions.

7.3. Comparison to Survey Runup Data

We compare modeled runup to observations from field surveys and optically derived runup distances in Figure 13. This figure shows runup and inundation height as a function of distance along the coast, subdivided in the western, southern (Palu City) and eastern coast. To improve visibility of the optically derived inundation distance, we apply a moving median filter of 250 m length, and show the 1–99 percentiles within this window as a measure of variability. In general terms our model produces comparable runup heights as reported from surveys, with maximum values around 8 m (around Watusampu at the west coast of the bay). Only around Wani and Pantoloan do we systematically underestimate the runup heights. The runup comparison also strongly favors models with a fault bend in the southern part of the bay, as scenarios *I, II, III* consistently overestimate runup in the north of the bay and underestimate runup heights along the southern bay coast (see Figure S16 in Supporting Information S1).

Inundation distances derived from satellite imagery agree well with inundation distances that we compute from surveyed locations. We model inundation distances in western Palu City that are comparable to those observed, but underestimate inundation distance at many other locations. We do not use reported flow depths because the DTM is at many places not representative for the coastal topography due to inclusion of vegetation and buildings.

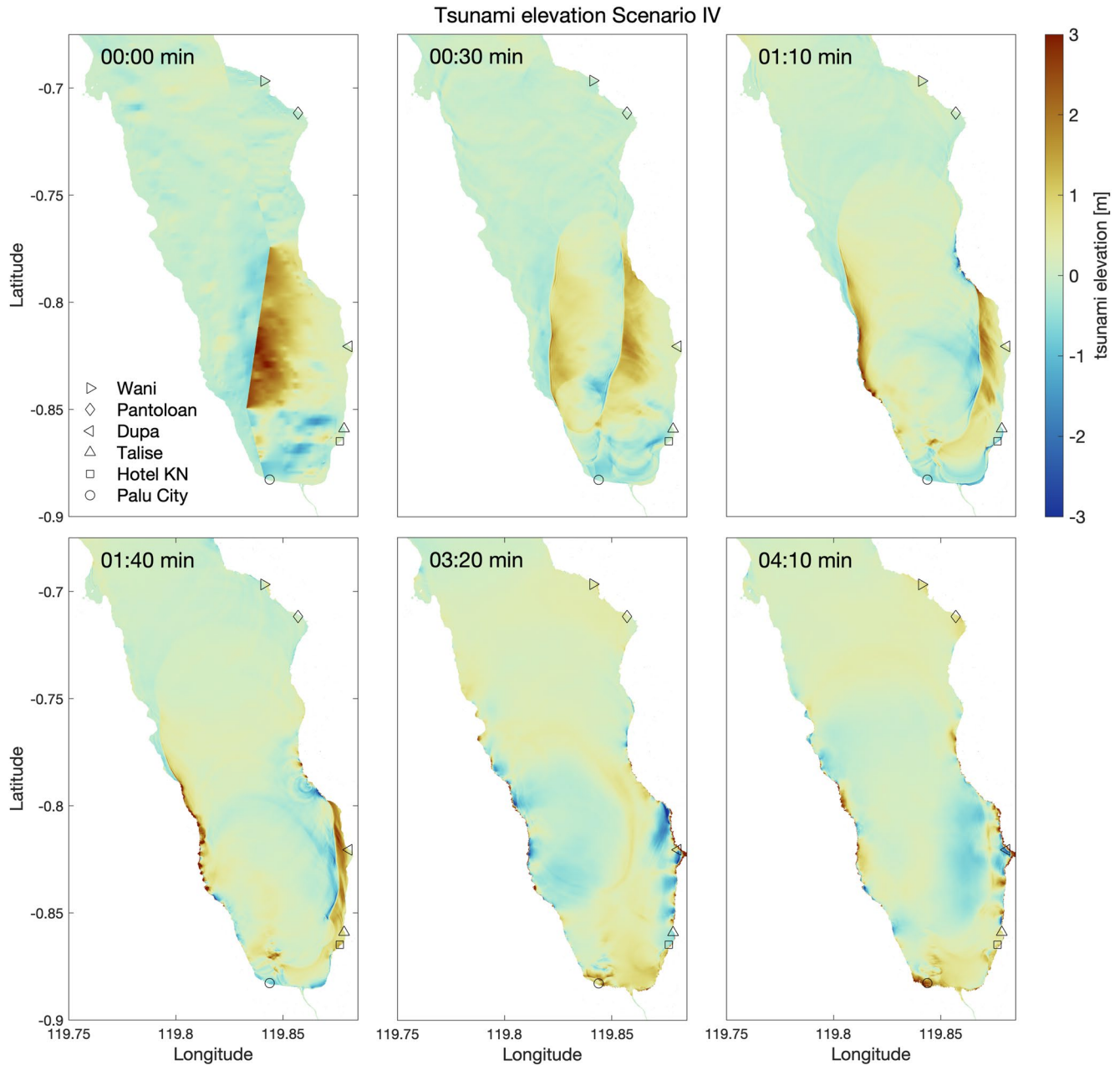


Figure 12. The evolution of the tsunami elevation (w.r.t. tide at the earthquake time) of scenario *IV* at six different epochs. The continuous evolution of the tsunami elevation can be found in Movie S1 in Supporting Information S1.

7.3.1. Robustness of the Preferred Scenario

Using the preferred *Scenario IV*, the uncertainties in the slip distribution have only a modest effect on the tsunami evolution, as Figure S19 in Supporting Information S1 shows that the MAP solution and the selection of extreme models have nearly identical tsunami model results. The timing, amplitude and polarity of the tsunami elevation is very similar compared to the MAP model, suggesting that under certain fault boundary conditions (i.e., the fault scenarios) the tsunami evolution is not very sensitive to uncertainties in slip distribution.

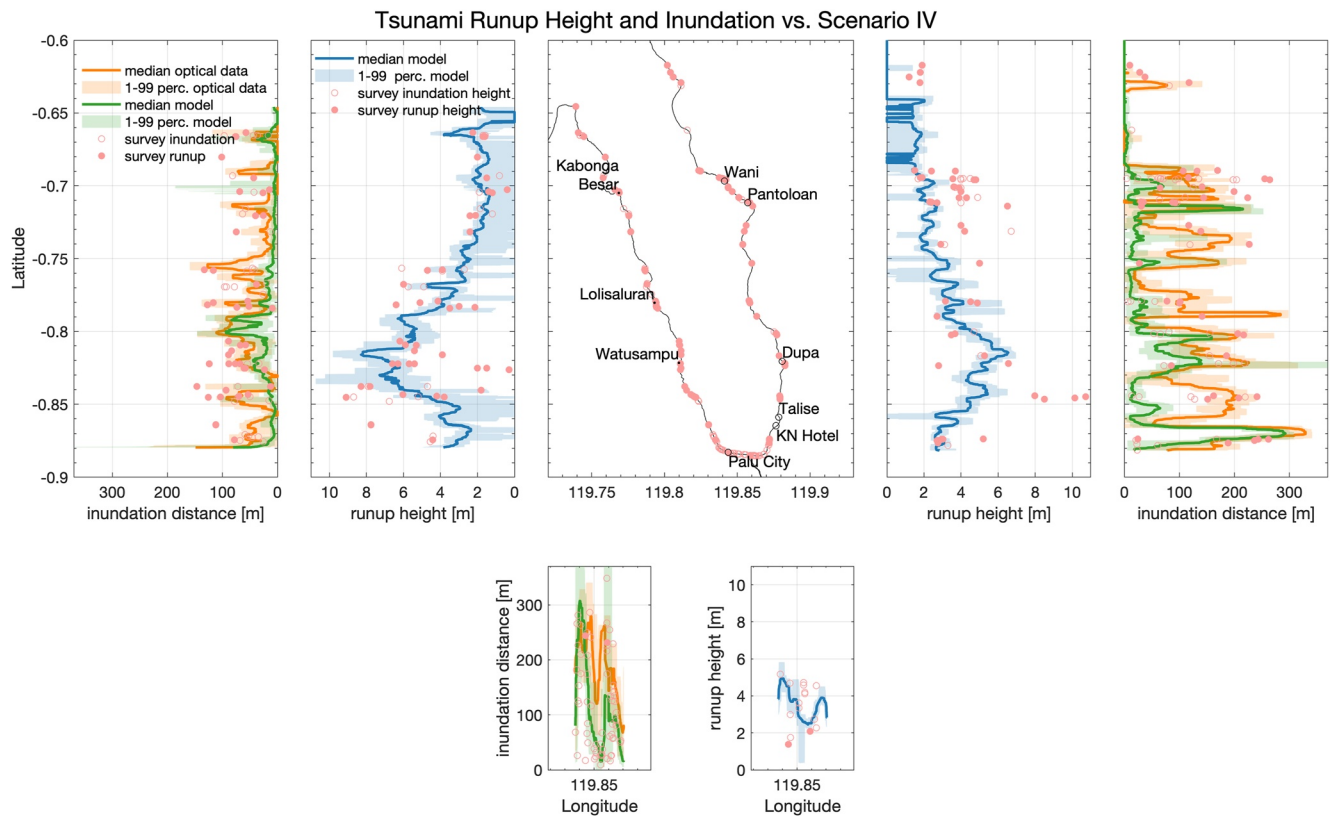


Figure 13. Comparison of observed runup height and inundation distance with results from the preferred *Scenario IV*. The middle panel shows the surveyed locations. The two left panels show modeled and observed the inundation distances, and the runup height at the west bay coast, respectively. The two right panels show the runup height and inundation distances for the southern bay coast, around Palu City. The inundation height and distances should be regarded as minimum values for that particular site. Surveyed runup heights and inundation distances are taken from Omira et al. (2019), Putra et al. (2019), Syamsidik et al. (2019), Mikami et al. (2019), Goda et al. (2019), Widiyanto et al. (2019). We apply a moving median filter to our optically derived inundation distance and to the modeled quantities (as a function of location at the coast), with a moving window of 250 m, and show the 1–99 percentile within this moving window.

8. Discussion

The 28 September 2018 M_w 7.5 Palu, (predominantly) strike-slip earthquake unexpectedly generated a tsunami in Palu Bay. In this study, we integrate a large set of geodetic data to determine a high-resolution 3D surface deformation field, invert for subsurface slip distributions for several plausible (offshore) finite fault scenarios, and compare consequent tsunami models with available observations. The subsequent sections consider the strengths and limitations of our approach and the available data, and our interpretation of these data compared to previous studies. Finally, we broaden the implications of transtensional and transpressional tectonics to the tsunamigenesis of strike-slip faults.

8.1. Resolving Co-seismic Displacements

8.1.1. Fault Trace

Our combination of co-seismic GPS and SAR data provides a view on the surface displacements that is complementary to earlier reports, but also uncovers previously unknown aspects. The north-south displacements, typical for a left-lateral strike-slip fault (Figure 3 or Figure S4 in Supporting Information S1 for the north component only), confirm earlier reports of offsets of a few meters on surface ruptures in Palu Valley, based on optical data (Bacques et al., 2020; He et al., 2019; Jamelot et al., 2019; Socquet et al., 2019; Sotiris et al., 2018). In our analysis the surface rupture is best resolved using the SAR azimuth offsets and MAI (see Figure S13 in Supporting Information S1). In the Sulawesi Neck we find no clear indication of a sharp surface rupture, which may either indicate that slip did not reach the surface or that the displacement occurred in a more distributed

sense by off-fault deformation. We do find strong indications of normal faulting, parallel to the main fault in the Sulawesi Neck that has not been reported previously. All GPS and SAR observations have been acquired within a few weeks after the earthquake: 1–42 days for a few GPS sites, and within 4–27 days for the SAR data. Nijholt et al. (2021) report post-seismic displacements on the order of a few cm in the first year since the event, which is two orders of magnitude smaller than the largest co-seismic estimates. So, while our observations are not purely co-seismic we expect relatively small contamination from post-seismic displacements. Still, the estimated normal faulting in the Sulawesi Neck is mostly based on SAR-displacement fields based on data 18–27 days after the actual earthquake, and the weighted root mean square misfit peaks around the inferred normal fault (see Figure S8 in Supporting Information S1). Hence, we cannot rule out that the activity observed off the main fault in the Sulawesi Neck has been an ongoing process unfolding during the observational period.

8.1.2. Tectonic Setting

The tectonic setting of the Palu Bay and Valley conforms to a transtensional basin: a main subsurface fault underlying the sedimentary basin(s) splays upward into distinct, small-scale fault strands in a negative flower structure (see Figure 5). The orientation of Riedel shear structures, which are commonly attributed to strike-slip faults (Figure 4), and the azimuth of interseismic velocities (Socquet et al., 2006) support that the main subsurface fault runs approximately parallel to the inferred fault traces at the Sulawesi Neck. Such an azimuth is in accordance with for example, Walpersdorf, Vigny, et al. (1998), and our deep fault orientation is different from the previously assumed offshore continuation along the west side of Palu Bay (Bellier et al., 2001, 2006; Natawidjaja et al., 2020). We concur with Stevens et al. (1999) that the deep, main fault trace is likely east of Palu Bay. While the overall setting is transtensional (Figure 5), we observe multiple onshore fault bends, both releasing bends leading to slip with a large normal component, as well as restraining bends that involve thrusting (Figure 7).

8.1.3. GPS Displacement Azimuth Variation

We find that the azimuths of the co-seismic displacements are mostly parallel to the average strike (350°). However, south of the bay, around Palu City, GPS co-seismic displacement vectors point consistently more to the west than elsewhere at comparable distances to the fault. These details in the displacement field are important for the interpretation of slip and fault geometry below the bay, where no direct observation of the surface displacement is possible. He et al. (2019) estimate a co-seismic 3D displacement field based on azimuth and range offsets from ALOS-2, from one ascending and one descending orbit and optical data from Sentinel-2. While they observe a similar displacement field as we present, their noise levels are higher, as SAR offsets and optical data have a lower precision than our data set. Therefore, the addition of GPS data is important to detect the deviating co-seismic displacement azimuth south of the bay.

8.1.4. Vertical Displacements

The vertical co-seismic displacement along the fault is generally minor; on the order of a few 10s of cm, see Figure 3. Only along fault bends, do we observe significant subsidence or uplift. Notably, along the southern releasing bend we observe up to 1.8 m subsidence (indicated in Figure 3 by *d*), which is well constrained by GPS site *PNDE*. Previously, there were no good constraints on the vertical co-seismic displacements, even though the lower signal-to-noise vertical displacement estimate from He et al. (2019) already hinted at significant subsidence north of the southern, releasing fault bend in Palu Valley. Similarly, Jaya et al. (2019) observed vertical offsets of 5 m at a surface rupture at the same location. Our estimated displacement field shows the spatial extent of these features. While smaller in magnitude, we observe notable uplift north of two restraining fault bends in the Sulawesi Neck, indicated by *e* in Figure 3.

Our study benefits from the combination of SAR and GPS data, and lacks the spurious displacements that are often found in the far-field results from optical data or SAR offset data. The large data set also allows us to observe secondary features, such as the subsidence and westward motion in the Sulawesi Neck, east of the main fault.

8.2. Inferred Slip Distribution

8.2.1. Shallowness of Rupture

The 2018 Sulawesi earthquake can be described as a generally shallow event; especially in Palu Valley, our slip inversion indicates that peak slip (up to 10 m) occurred in the upper 7 km with significant slip right up to the

surface. While localized slip does not seem to have reached the surface in the Sulawesi Neck, slip prevails in the upper 7 km. Only at a few isolated locations does our inversion put relatively large (>5 m) slip below 7 km on the deeper, straight fault segment. This is a similar picture as in Socquet et al. (2019), Williamson et al. (2020), He et al. (2019), Bacques et al. (2020), where the latter two studies also find a lack of very shallow slip below the Sulawesi Neck. While seismological inversions recover a large slip asperity in the southern portion of the rupture, some studies place the large slip area too far north, in the bay rather than in Palu Valley (USGS, 2018; Yolsal-Çevikbilen & Taymaz, 2019). As Lee et al. (2019) show, seismological slip solutions can be more in agreement with geodesy around the location of the large slip in the southern part of the rupture when allowing higher rupture velocities. Generally, slip models based on seismological data confirm that the peak slip during the event was shallow (<10 km) (Fang et al., 2019; Li et al., 2020; Zhang et al., 2019). The shallow depths of the rupture agree well with the interseismic locking in the upper 12 km only, as inferred from GPS data (Socquet et al., 2006). As the local crustal velocity structure is unknown, we rely on homogenous elastic models in the slip inversion. The assumption of homogeneity generally leads to slight biases in estimated slip depth for typical elastic heterogeneities, while the spatial distribution remains similar (Hooper et al., 2002; Ragon & Simons, 2021).

8.2.2. Sensitivity of the Geodetic Data to Sub-Bay Slip

Whereas co-seismic uplift from thrusting below the bay cannot be observed directly, we infer thrusting on a restraining fault bend below the bay, connecting the clearly observable north and south onshore fault strands, to explain GPS and SAR displacements (Figure 9). Thrusting below the bay has been proposed before by Socquet et al. (2019) and He et al. (2019), but most previous fault slip solutions for the Palu earthquake have been hampered by lack of constraints on vertical deformation, or have relied on north-south displacements only. A discontinuous rupture in the form of a step-over has previously been explored by Wang et al. (2019) and Williamson et al. (2020). We consider that a step-over is unlikely, as even in scenario VI where we prescribe a discontinuous fault below the bay, the southern bay segment shows behavior more typical for fault bends: it contains a proportion of dip-slip and it trends NNE rather than NNW as what would correspond to sub-parallel faults at both sides of a step-over (see Figure 9). As Figure 10 shows, uplift of more than 2 m concentrates above the fault bend segments (when bends are included in the scenario). In other published fault models, such large dip-slip, and accompanying uplift, is either lacking (Wang et al., 2019; Williamson et al., 2020; Bacques et al., 2020) or has a smaller magnitude (He et al., 2019; Jamelot et al., 2019; Sepúlveda et al., 2020; Socquet et al., 2019).

8.2.3. Fault Dip Angles

Our estimated dip angle of the thrust segments ($45\text{--}50^\circ$, Figure 8) is considerably smaller than the large dip angles in other studies: $70\text{--}90^\circ$ (Sepúlveda et al., 2020); 60° (Socquet et al., 2019); 65° (Ulrich et al., 2019); 70° (He et al., 2019). The subdivision of our fault model into a shallow and deep part allows a gentler dip angle in the shallow parts, and a steep dip for the deep fault. The dip-angle has a large influence on balance between the estimated uplift and subsidence below the bay. For example, large dip angles lead to symmetrical uplift and subsidence magnitudes (Bacques et al., 2020; Ulrich et al., 2019). Comparable dips are only found in Jamelot et al. (2019), who find a preference for a 45° dip angle for the fault bend—in a setup similar to Scenario I—which leads to predominant uplift and only minor subsidence above the deeper parts of the rupture. Only the onshore fault segments in the north of the Sulawesi Neck (K, L) favor contrastingly large dip angles (comparable to the USGS moment tensor solution with a 66° dip (USGS, 2018)). The seismological dip angle solution may represent an average dip between the dip angle of the shallow segments and that of the deep segment, for which we estimate smaller and larger dip angles, respectively. The very steep dip angles observed by Jaya et al. (2019) from surface ruptures (in the range $70\text{--}85^\circ$) do not seem to be representative for the fault of the upper 7 km. We find a single case of westward dip, in the southernmost part of the rupture. As we use straight fault planes, a gradual change in dip angle going from the shallow segments to the deep fault is not possible, such as in the sketch of the negative flower structure in Figure 5. This means that we only obtain an approximate continuation from the shallow segments to the vertical deep fault segment.

8.3. Tsunami Potential of the Co-seismic Displacements

On the basis of the fault model by Socquet et al. (2019), Carvajal et al. (2019) argue that a tsunami driven by deformation due to fault slip cannot match the observed tsunami amplitude. Similar arguments have been put forward by Heidarzadeh et al. (2019) and Jamelot et al. (2019) regarding insufficient model runup compared to

observed runup heights by post-tsunami surveys. A number of studies propose landslides as the (partial) source for the tsunami (Gusman et al., 2019; Nakata et al., 2020; Pakoksung et al., 2019; Sepúlveda et al., 2020; Takagi et al., 2019; Williamson et al., 2020). Schambach et al. (2020) model tectonic (using models from Socquet et al. (2019); Jamelot et al. (2019); Ulrich et al. (2019)) and landslide tsunami sources, where the latter are based on pre- and post-earthquake bathymetry analyses of Liu et al. (2020). We argue that the proposed landslide dominance of the tsunami is tentative, mostly due to the fact that previous finite fault slip models have underestimated the uplift due to dip-slip below the bay. Furthermore, most landslide sources are rather speculative, and the timing of the landslide sources is unconstrained. Liu et al. (2020) study bathymetry changes between pre-earthquake surveys from 2014, 2015 and 2017 and post-earthquake surveys conducted in October and November 2018. Differences between the 2014 or 2015 bathymetry and the post-earthquake bathymetry reveal bathymetry changes (>50 m) that are much larger than the changes at presumed submarine landslide locations, and results from 2014 are not consistent with those from 2015. On the other hand, the 2017 survey only covers a small part of the northern bay (close to Pantoloan), but differences with the post-earthquake survey are much more localized, providing reasonable indications for at least two sub-marine landslides close to Wani and Pantoloan.

While we do not rule out contributions from landslides, or more specifically, sub-marine landslides, our models show that displacements due to co-seismic slip are most likely the major tsunami source. This applies especially to the stretch of coast between Palu City northeastwards to Dupa, where timing constraints on the first tsunami arrival are available. Along the southeastern coast, all tested scenarios that explain the geodetic observations lead to runup heights that are of the same order as what has been observed by post-earthquake surveys. An interesting feature of the video analysis of Carvajal et al. (2019) is the early (1–2 min) arrival of the first tsunami waves in the southeast coast of the bay (Hotel KN, Talise and Dupa) compared to more northern sites at the eastern coast (Pantoloan, Wani) (3 min) suggesting a source within the southern part of the Bay. Takagi et al. (2019) proposed (submarine) landslide sources at the western bay coast, but modeled arrival times for the southeastern coast at the video waveform locations are 1–2 min too late. Similar results can be found in Liu et al. (2020) and Schambach et al. (2020), where landslide-only tsunami models cannot explain arrival times in the southeastern bay coast. Alternatively, all our models reproduce the arrival times and polarity in this area (Hotel KN, Talise, and Dupa, Figure 11), even though our arrival times may be off by 30 s. This leaves open slight deviations in exact uplift locations, but requires a location within the bay, rather than submarine landslides at the western bay coast.

At the west coast, our preferred fault scenario predicts very early arrival of the tsunami waves, at around 1:30 min, see Figure 12. The features that look like rings of sea surface elevation at the western bay coast, as photographed from an airplane 1:50 min after the event, have been interpreted as landslide sources by Carvajal et al. (2019), where the smallest photographed features appear to be located at the coast. Still, our model also produces similar features after the first waves hit the coast and reflect after 1:40 min (Figure 12, and Movie S1 in Supporting Information S1).

Contrastingly, we have not been able to find fault geometries that can explain the relatively late arrival of tsunami waves at Pantoloan and Wani, even though these sites are quite close to the location where the rupture has entered the bay from the Sulawesi Neck. Models with uplift above the northern sub-bay segment of the fault (scenarios *I*, *II*, *III*) always lead to an overly early arrival at Pantoloan. Previously, results from Ulrich et al. (2019); Jamelot et al. (2019); Williamson et al. (2020); Schambach et al. (2020) illustrate the difficulty to explain the Pantoloan tsunami arrival times when the co-seismic source is close to the location where the rupture entered the bay. As an exception, Gusman et al. (2019) propose a co-seismic vertical displacement field that places Pantoloan exactly at the hinge line that divides an area of uplift from a subsiding area, but it is difficult to relate this long-wavelength displacement field to a tectonic source. Late tsunami arrival in Pantoloan naturally places the fault bend more southerly in the bay. In scenarios *IV*, *V*, *VI* we used the 170 s travel time contour of Carvajal et al. (2019) to locate areas of significant vertical displacements. Such a southern fault bend location, however, does not explain 2 m waves observed at Pantoloan and Wani, since largest waves travel perpendicularly to the fault bend (roughly east-west), rather than toward the north. Also the observed negative polarity of the first arrival at Pantoloan poses a problem, as all our model scenarios predict a positive wave traveling to all coasts, because of the predominance of uplift compared to subsidence (similar to models from Sepúlveda et al. (2020); Williamson et al. (2020); Schambach et al. (2020)). This leaves the option open for other sources, such as tsunami waves generated by landslides, especially sites close to Pantoloan, as advocated by Liu et al. (2020) and Schambach et al. (2020). From the bathymetric study by Liu et al. (2020) there are indications for such landslides, and assuming a 75 s delay compared to the rupture time Schambach et al. (2020) find a good agreement with the video waveforms at

Wani and Pantoloan based on landslide sources only. On the other hand, based on the same landslide sources, Liu et al. (2020) have difficulty in explaining the arrival of the second, positive waves in Wani and Pantoloan, which suggests a significant sensitivity to the exact parametrization of the landslide sources.

Seismological studies report that the Palu earthquake rupture propagated at speeds higher than the shear wave velocity, also known as a supershear rupture (Amlani et al., 2022; Bao et al., 2019; Li et al., 2020; Ulrich et al., 2019). Coupled rupture and tsunami models show that tsunami wave timing and magnitude is relatively insensitive to rupture speed (sub-shear or super-shear speed) when the static fault slip is similar (Elbanna et al., 2021). Furthermore, the long wave period (~0.5 min) and largest amplitude waves are still generated by the permanent co-seismic deformation, just as for earthquakes rupturing at sub-shear speeds (Maeda & Furumura, 2013; Ohmachi et al., 2001). As our geodetic observations actually constrain the offshore permanent co-seismic displacements, we already capture the relevant features of the tectonically induced tsunami waves.

As the only available topography data are based on a digital terrain model, that includes vegetation, our model has difficulties explaining the inundation distances such as observed by post-tsunami surveys, as our onshore topography is biased. Tests with lower friction values of the sea bed (for a definition see Section 5) do not lead to significant different inundation distances. We are not aware of any other study to the Palu tsunami that compares modeled with observed inundation distances.

8.4. Relevance for Other Transtensional Basins

In recent years, an increasing number of tsunamis have been related to (the direct consequences of co-seismic strike-slip events, that is, offshore the Philippines (Imamura et al., 1995), offshore Canada (Rabinovich et al., 2008), within the Sea of Marmara (Altunok & Ersoy, 2000), near and along Haiti (Hornbach et al., 2010; Poupardin et al., 2020), at the San Andreas fault (Geist & Zoback, 1999), in New Zealand (King, 2015), at Wharton Basin (Gusman et al., 2017) and within the Gulf of Aqaba (Frucht et al., 2019; Ribot et al., 2021). This includes settings where strike-slip earthquakes caused tsunamigenic aftershock activity on nearby fault systems (Geist & Parsons, 2005; ten Brink et al., 2020). Notably, strike-slip faults can constitute multiple fault segments at shallow levels, especially in the case of transtensional basins. This thus means that an earthquake rupture in such settings is likely to create localized, vertical, submarine motions able to generate significant tsunamis (Cormier et al., 2006; Geist & Zoback, 1999). Previously, activity on several fault strands has often been argued to be insufficient to explain observed inundation and runup of tsunamis completely (Cormier et al., 2006; Öztürk et al., 2000), hence the requirement of a secondary tsunami source. In literature, there are abundant relations between earthquakes and (induced) submarine mass movements (for example, Hornbach et al., 2010; McHugh, Seeber, et al., 2014; Yalçiner et al., 2002).

We recognize that the transtensional tectonic setting of Palu Bay (Figure 5) is very similar to the well-studied Sea of Marmara and Gulf of Izmit regions of the North Anatolian fault, in that multiple fault strands run across and below the basins in a negative flower setting (Aksu et al., 2000; Laigle et al., 2008; Yalçiner et al., 2002). Many tsunamis have been identified and attributed to extensive tectonic activity in the Marmara Sea region (e.g., Altunok et al., 2011; Yalçiner et al., 2002). For example, a multitude of dated submarine mass movements in the Marmara Sea correlate well with documented historical earthquake ruptures (e.g., Çağatay et al., 2012; Drab et al., 2012; McHugh, Braudy, et al., 2014). However, in their extensive catalog, Altunok et al. (2011) only ascribe a limited amount of reported tsunamis to finite fault ruptures. Studies using tsunami modeling in the Marmara Sea point toward a larger potential of (local) destructive tsunami run-up due to (submarine) landslides compared to co-seismic fault ruptures (Hébert et al., 2005; Latcharote et al., 2016). Still, these studies include very crude (generic) slip distributions on simple fault geometries. Tinti et al. (2006), on the other hand, conclude that the tsunamigenic potential in the Gulf of Izmit reasonably matches tsunami observations across the shoreline for co-seismic ruptures that include a fault bend zone: smaller scale faults with dip-slip motion in between (longer) segments that host dominant strike-slip motion. The importance of submarine bends, or step-overs, in a strike-slip fault zone thus rivals that of (submarine) landslides. Landslide contributions may then be expressed as local (secondary) features in the tsunami observations (e.g., Tinti et al., 2006). Analysis of sediments along basin-bounding faults at the Sea of Marmara reveals co-seismic vertical offsets of up to 1.8 m (Beck et al., 2015). Such offsets are more than enough reason to consider the dip-slip component of any segment in a transtensional basin.

A large strike-slip earthquake is likely to include a rupture across several fault segments, incorporating slip on fault bends, especially when occurring in a transtensional basin. Fault bends can also act as impeding features for earthquake ruptures and fault segments active on a geological time scale are not necessarily activated every single time an earthquake rupture front approaches them (Biasi & Wesnousky, 2016). For example, the Hershek restrictive bend connects two main segments of the North Anatolian northern fault strand in the Sea of Marmara and the Gulf of Izmit. The notion of a continuous surface-breaking rupture during the 1999 Izmit earthquake is debated, and the subsidence history over the past two millennia indicates that not every major, tsunamigenic earthquake that affected this bend resulted in surface-breaking differential motion across the fault interface (e.g., Bertrand et al., 2011; Lettis et al., 2002; Özaksoy et al., 2010). Fault bend activity, or vertical motion due to geometrical steps, is highly dependent on the activity on its adjacent segments.

The presence of (submarine) fault bends or step-overs is likely in a transtensional setting, yet estimates of slip distributions on such (sometimes relatively small and offshore) bends are largely lacking in the literature due to the absence of direct observations of slip on fault bends. Therefore, it is likely that their contribution to co-seismic vertical displacements has often been overlooked. For Palu Bay the geodetic data support significant co-seismic uplift offshore on a restraining fault bend, whereas the breath of geodetic observations do not show large vertical displacements onshore on either side of Palu Bay. This restraining bend behavior is comparable to the up to 1.8 m subsidence on an onshore releasing bend in southern Palu Valley. Our study concurs with Tinti et al. (2006) in suggesting that fault bends and step-overs may play a large role in generating tsunamis in transtensional basins, whereas (submarine) landslide contributions complement the picture locally.

9. Conclusions

Based on our integration of GPS and SAR co-seismic displacements, we conclude that the continuous, 3D, co-seismic displacement field resolves many features of the 2018 Palu earthquake. This includes a sharp surface rupture in Palu Valley, but an absence of a displacement discontinuity in the Sulawesi Neck. The observations are consistent with a continuous left-lateral strike-slip fault system. We interpret the geodetic data with a Bayesian fault inversion, and observe a number of fault bends and a secondary fault in the Sulawesi Neck that we attribute to normal faulting. The Palu-Koro Fault is a continuous and single near-vertical fault below ~ 7 km depth, that branches into multiple semi-parallel fault segments toward shallower depth levels. A strike of 350° for the deep part of the fault underlying the shallow faults forming the 2018 rupture is consistent with the orientations of faults in the Palu-Koro fault region, and with interseismic velocities. Still, we find that most of the slip occurred at shallow (< 7 km) depths. The magnitude of displacement is generally larger east of the fault, and our inversion suggests for most segments a dip angle in the range 45° – 50° .

The observed fault bends and the inferred fault bend underneath Palu Bay conform to our interpretation of the tectonic setting as a transtensional basin. Our observations suggest transtensional co-seismic subsidence as well as transpressional uplift on shallow fault bends. The fault bends that connect the straight, dominantly strike-slip segments of the rupture have accommodated significant dip-slip motion during the earthquake. Below the bay, our model predicts uplift of the sea floor up to 2–3 m due to dip-slip on an inferred fault bend, which connects the northern fault segment in the Sulawesi Neck and the approximately parallel fault segment south in Palu Valley.

Combining the inversion results with a tsunami model, we conclude that the tsunami arrival times and wave polarity from amateur and CCTV videos in the south and southeastern part of the bay can be described with a co-seismic uplift source in the Bay. The modeled tsunami, based on the finite fault, produces a spatial distribution and magnitude of runup that is close to the survey data along the coastline of Palu Bay. From the various tested fault geometry scenarios below the Bay, the comparison of the model with tsunami data favors a relatively southerly location in the Bay. While the majority of tsunami observations can be explained by fault slip alone, the observed timing of the tsunami and the runup around Pantoloan and Wani are difficult to match with a co-seismic source, and are possibly caused by non-tectonic bathymetry changes. Irrespective of local effects, our data and modeling indicate that fault bends have played a major role in the tsunamigenesis of the 2018 Palu earthquake; fault bends may be equally important to consider for tsunami hazards in comparable strike-slip settings.

Data Availability Statement

The data underlying this manuscript and model results are available at the 4TU Research data repository (<https://data.4tu.nl>) (<https://doi.org/10.4121/19168442>). These data and results include: the GPS kinematic time series, GPS co-seismic displacement tables, raw GPS RINEX files, inundation contours, the data reduced SAR displacement fields, 3D displacement field estimate and corresponding displacement inversion input files, finite fault solution (map solution for each fault scenario), combined bathymetry-topography, and the vertical displacement fields for the finite fault solution of scenario IV. The satellite imagery that we use to estimate tsunami inundation is available at: <https://www.maxar.com/open-data/indonesia-earthquake-tsunami>. We have made use of color-maps by Colorbrewer and Fabio Cramer (Cramer, 2018).

The software for this study is partly open access, as specified below:

- QGIS as used for the analysis of tsunami inundation is open access software (<https://www.qgis.org>).
- A research license for the GPS processing software GIPSY-OASIS II can be obtained at <https://gipsy-oasis.jpl.nasa.gov>.
- The Geodetic Bayesian Inversion Software GBIS is written in Matlab and is freely accessible at <https://comet.nerc.ac.uk/downloadgbis>.
- H2Ocean is open source software and is freely accessible at <https://github.com/OKleptsova/H2Ocean.git>.
- GSISAR used for SAR processing is not accessible to the public or research community under the policy of GSI.

References

- Abendanon, E. (1915). *Geologische en geografische doorkruizingen van Midden Celebes. Bd. I–IV*. Leiden.
- Aksu, A. E., Calon, T. J., Hiscott, R. N., & Yasar, D. (2000). Anatomy of the North Anatolian fault zone in the Marmara Sea, Western Turkey: Extensional basins above a continental transform. *Geological Society of America Today*, 10(6), 3–7.
- Altunok, Y., Alpar, B., Özer, N., & Aykurt, H. (2011). Revision of the tsunami catalogue affecting Turkish coasts and surrounding regions. *Natural Hazards and Earth System Sciences*, 11(2), 273–291. <https://doi.org/10.5194/nhess-11-273-2011>
- Altunok, Y., & Ersoy, Ş. (2000). Tsunamis observed on and near the Turkish coast. In *Natural hazards* (pp. 185–205). Springer. https://doi.org/10.1007/978-94-017-2386-2_5
- Amlani, F., Bhat, H. S., Simons, W. J., Schubnel, A., Vigny, C., Rosakis, A. J., et al. (2022). Supershear shock front contribution to the tsunami from the 2018 M_w 7.5 Palu, Indonesia earthquake. *Geophysical Journal International*, 230(3), 2089–2097. <https://doi.org/10.1093/gji/ggac162>
- Arikawa, T., Muhari, A., Okumura, Y., Dohi, Y., Afriyanto, B., Sujatmiko, K. A., & Imamura, F. (2018). Coastal subsidence induced several Tsunamis during the 2018 Sulawesi Earthquake. *Journal of Disaster Research*, 13(Scientific Communication), sc20181201. <https://doi.org/10.20965/jdr.2018.sc20181201>
- Bacques, G., de Michele, M., Foulmelis, M., Raucoules, D., Lemoine, A., & Briole, P. (2020). Sentinel optical and SAR data highlights multi-segment faulting during the 2018 Palu-Sulawesi earthquake (M_w 7.5). *Scientific Reports*, 10(1), 1–11. <https://doi.org/10.1038/s41598-020-66032-7>
- Bagnardi, M., & Hooper, A. (2018). Inversion of surface deformation data for rapid estimates of source parameters and uncertainties: A Bayesian approach. *Geochemistry, Geophysics, Geosystems*, 19(7), 2194–2211. <https://doi.org/10.1029/2018gc007585>
- Bao, H., Ampuero, J.-P., Meng, L., Fielding, E. J., Liang, C., Milliner, C. W., et al. (2019). Early and persistent supershear rupture of the 2018 magnitude 7.5 Palu earthquake. *Nature Geoscience*, 12(3), 200–205. <https://doi.org/10.1038/s41561-018-0297-z>
- Bechor, N. B. D., & Zebker, H. A. (2006). Measuring two-dimensional movements using a single InSAR pair. *Geophysical Research Letters*, 33(16), L16311. <https://doi.org/10.1029/2006GL026883>
- Beck, C., Campos, C., Eriş, K., Çağatay, N., Mercier de Lepinay, B., & Jouanne, F. (2015). Estimation of successive coseismic vertical offsets using coeval sedimentary events—Application to the southwestern limit of the Sea of Marmara’s Central Basin (North Anatolian Fault). *Natural Hazards and Earth System Sciences*, 15(2), 247–259. <https://doi.org/10.5194/nhess-15-247-20>
- Bellier, O., Beaudouin, T., Sebrier, M., Villeneuve, M., Bahar, I., Putranto, E., et al. (1998). Active faulting in central Sulawesi (eastern Indonesia). In *GEODYSSSEA project final report* (pp. 98–14).
- Bellier, O., Sébrier, M., Beaudouin, T., Villeneuve, M., Braucher, R., Bourles, D., et al. (2001). High slip rate for a low seismicity along the Palu-Koro active fault in central Sulawesi (Indonesia). *Terra Nova*, 13(6), 463–470. <https://doi.org/10.1046/j.1365-3121.2001.00382.x>
- Bellier, O., Sébrier, M., Seward, D., Beaudouin, T., Villeneuve, M., & Putranto, E. (2006). Fission track and fault kinematics analyses for new insight into the Late Cenozoic tectonic regime changes in West-Central Sulawesi (Indonesia). *Tectonophysics*, 413(3–4), 201–220. <https://doi.org/10.1016/j.tecto.2005.10.036>
- Bertrand, S., Doner, L., Akçer Ön, S., Sancar, U., Schudack, U., Mischke, S., et al. (2011). Sedimentary record of coseismic subsidence in Hersek coastal lagoon (Izmit bay, Turkey) and the late Holocene activity of the North Anatolian fault. *Geochemistry, Geophysics, Geosystems*, 12(6), 1–9. <https://doi.org/10.1029/2011GC003511>
- Biasi, G. P., & Wesnousky, S. G. (2016). Steps and gaps in ground ruptures: Empirical bounds on rupture propagation. *Bulletin of the Seismological Society of America*, 106(3), 1110–1124. <https://doi.org/10.1785/0120150175>
- Bradley, K., Mallick, R., Andikagumi, H., Hubbard, J., Meilianda, E., Switzer, A., et al. (2019). Earthquake-triggered 2018 Palu Valley landslides enabled by wet rice cultivation. *Nature Geoscience*, 12(11), 935–939. <https://doi.org/10.1038/s41561-019-0444-1>
- Çağatay, M., Erel, L., Bellucci, L., Polonia, A., Gasperini, L., Eriş, K., et al. (2012). Sedimentary earthquake records in the Izmit gulf, sea of Marmara, Turkey. *Sedimentary Geology*, 282, 347–359. <https://doi.org/10.1016/j.sedgeo.2012.10.001>
- Carvajal, M., Araya-Cornejo, C., Sepúlveda, I., Melnick, D., & Haase, J. S. (2019). Nearly-instantaneous tsunamis following the M_w 7.5 2018 Palu earthquake. *Geophysical Research Letters*, 46(10), 5117–5126. <https://doi.org/10.1029/2019gl082578>

Acknowledgments

Some specifications to the CReDiT contributions. Data curation concerns collecting GPS data and maintaining the GPS network. For the formal analysis, W.S. has processed the GPS data and Y.M. has performed the SAR-data processing; W.S. and M.N. combined bathymetric and topographic data. T.B. has led the investigation process and has combined the different co-seismic displacement datasets into the combined displacement field; L.S. has conducted the finite fault inversion; O.K. has performed the tsunami modeling; N.N. has analyzed the fault directions; S.L. has analyzed the inundation on basis of optical data. T.B. has taken lead in writing the manuscript, supported by N.N. The continued (long-term) operation of the GPS stations in Central Sulawesi has been co-facilitated by the EU-ASEAN SEAMERGES (2004–2006) and GEO2TECDI-1/2 projects (2009–2013). The GPS data acquisition and research were also partly funded by grants from the Dutch NWO User Support Programme Space Research (2007–2023). A special thanks to our local survey staff Rahman Umar and Urip for their continued support, including the inspection of the GPS stations directly after the earthquake. ALOS-2 data were provided under a cooperative research contract between GSI and JAXA. The ownership of ALOS-2 data belongs to JAXA. Taco Broerse is funded by NWO grant ALWGO.2018.038. Olga Kleptsova was initially funded by a 2 months PD grant awarded to J. Pietrzak by the Department of Hydraulic Engineering, TU Delft which is gratefully acknowledged. Matthew Herman was funded by The Netherlands Research Centre For Integrated Solid Earth Science, grant ISES 2017-UU-22. COMET is the UK Natural Environment Research Council’s Centre for the Observation and Modelling of Earthquakes, Volcanoes and Tectonics. We would like to dedicate our research work in memory of all casualties of the 2018 Palu earthquake. This includes Maya Pasau, who helped us with setting up one of the GNSS stations, her husband Yudi and their children Fiki and Ai who tragically lost their lives when the tsunami struck Talise beach. Furthermore, we thank Jeffrey Freymueller, two anonymous reviewers, editor Isabelle Manighetti and associate editor Alice-Agnes Gabriel for their helpful reviews and suggestions to improve the manuscript.

- Cipta, A., Robiana, R., Griffin, J., Horspool, N., Hidayati, S., & Cummins, P. R. (2017). A probabilistic seismic hazard assessment for Sulawesi, Indonesia. *Geological Society, London, Special Publications*, 441(1), 133–152. <https://doi.org/10.1144/sp441.6>
- Cormier, M.-H., Seeber, L., McHugh, C. M., Polonia, A., Çagatay, N., Emre, Ö., et al. (2006). North Anatolian Fault in the Gulf of Izmit (Turkey): Rapid vertical motion in response to minor bends of a nonvertical continental transform. *Journal of Geophysical Research*, 111(B4), B04102. <https://doi.org/10.1029/2005JB003633>
- Crameri, F. (2018). Scientific colour-maps. <https://doi.org/10.5281/zenodo.1243862>
- Crowell, J. (1974). *Origin of late Cenozoic basins in southern California*. Society of Economic Paleontologists and Mineralogists Special Publication No. 22.
- Cui, H., Pietrzak, J., & Stelling, G. (2010). A finite volume analogue of the P1NC-P1 finite element: With accurate flooding and drying. *Ocean Modelling*, 35(1), 16–30. <https://doi.org/10.1016/j.ocemod.2010.06.001>
- Cui, H., Pietrzak, J., & Stelling, G. (2012). Improved efficiency of a non-hydrostatic, unstructured grid, finite volume model. *Ocean Modelling*, 54–55, 55–67. <https://doi.org/10.1016/j.ocemod.2012.07.001>
- Cui, H., Pietrzak, J., & Stelling, G. (2014). Optimal dispersion with minimized Poisson equations for non-hydrostatic free surface flows. *Ocean Modelling*, 81, 1–12. <https://doi.org/10.1016/j.ocemod.2014.06.004>
- Cunningham, W., & Mann, P. (2007). Tectonics of strike-slip restraining and releasing bends. *Geological Society, London, Special Publications*, 290(1), 1–12. <https://doi.org/10.1144/sp290.1>
- Decriem, J., Arnadóttir, T., Hooper, A., Geirsson, H., Sigmundsson, F., Keiding, M., et al. (2010). The 2008 May 29 earthquake doublet in SW Iceland. *Geophysical Journal International*, 181(2), 1128–1146. <https://doi.org/10.1111/j.1365-246x.2010.04565.x>
- Drab, L., Hubert Ferrari, A., Schmidt, S., & Martinez, P. (2012). The earthquake sedimentary record in the western part of the Sea of Marmara, Turkey. *Natural Hazards and Earth System Sciences*, 12(4), 1235–1254. <https://doi.org/10.5194/nhess-12-1235-2012>
- Elbanna, A., Abdelmeguid, M., Ma, X., Amlani, F., Bhat, H. S., Synolakis, C., & Rosakis, A. J. (2021). Anatomy of strike-slip fault tsunami genesis. *Proceedings of the National Academy of Sciences*, 118(19), e2025632118. <https://doi.org/10.1073/pnas.2025632118>
- Fang, J., Xu, C., Wen, Y., Wang, S., Xu, G., Zhao, Y., & Yi, L. (2019). The 2018 M_w 7.5 Palu Earthquake: A supershear rupture Event constrained by InSAR and broadband regional Seismograms. *Remote Sensing*, 11(11), 1330. <https://doi.org/10.3390/rs11111330>
- Frucht, E., Salamon, A., Gal, E., Ginat, H., Grigorovitch, M., Tov, R. S., & Ward, S. (2019). A fresh view of the tsunami generated by the Dead Sea Transform, 1995 M_w 7.2 Nuweiba earthquake, along the gulf of Elat–Aqaba. *Seismological Research Letters*, 90(4), 1483–1493. <https://doi.org/10.1785/0220190004>
- Geist, E. L., & Parsons, T. (2005). Triggering of tsunamigenic aftershocks from large strike-slip earthquakes: Analysis of the November 2000 New Ireland earthquake sequence. *Geochemistry, Geophysics, Geosystems*, 6(10), Q10005. <https://doi.org/10.1029/2005GC000935>
- Geist, E. L., & Zoback, M. L. (1999). Analysis of the tsunami generated by the M_w 7.8 1906 San Francisco earthquake. *Geology*, 27(1), 15–18. [https://doi.org/10.1130/0091-7613\(1999\)027<0015:AOTTGB>2.3.CO;2](https://doi.org/10.1130/0091-7613(1999)027<0015:AOTTGB>2.3.CO;2)
- Goda, K., Mori, N., Yasuda, T., Prasetyo, A., Muhammad, A., & Tsujio, D. (2019). Cascading geological hazards and risks of the 2018 Sulawesi Indonesia earthquake and sensitivity analysis of tsunami inundation simulations. *Frontiers of Earth Science*, 7, 261. <https://doi.org/10.3389/feart.2019.00261>
- Gusman, A. R., Satake, K., & Harada, T. (2017). Rupture process of the 2016 Wharton Basin strike-slip faulting earthquake estimated from joint inversion of teleseismic and tsunami waveforms. *Geophysical Research Letters*, 44(9), 4082–4089. <https://doi.org/10.1002/2017GL073611>
- Gusman, A. R., Supendi, P., Nugraha, A. D., Power, W., Latief, H., Sunendar, H., et al. (2019). Source model for the Tsunami inside Palu bay following the 2018 Palu earthquake, Indonesia. *Geophysical Research Letters*, 46(15), 8721–8730. <https://doi.org/10.1029/2019gl082717>
- Harding, T. P. (1985). Seismic characteristics and identification of negative flower structures, positive flower structures, and positive structural inversion. *AAPG Bulletin*, 69(4), 582–600.
- He, L., Feng, G., Li, Z., Feng, Z., Gao, H., & Wu, X. (2019). Source parameters and slip distribution of the 2018 M_w 7.5 Palu, Indonesia earthquake estimated from space-based geodesy. *Tectonophysics*, 772, 228216. <https://doi.org/10.1016/j.tecto.2019.228216>
- Hébert, H., Schindele, F., Altnok, Y., Alpar, B., & Gazioglu, C. (2005). Tsunami hazard in the Marmara Sea (Turkey): A numerical approach to discuss active faulting and impact on the Istanbul coastal areas. *Marine Geology*, 215(1–2), 23–43. <https://doi.org/10.1016/j.margeo.2004.11.006>
- Heidarzadeh, M., Muhari, A., & Wijanarto, A. B. (2019). Insights on the source of the 28 September 2018 Sulawesi tsunami, Indonesia based on spectral analyses and numerical simulations. *Pure and Applied Geophysics*, 176(1), 25–43. <https://doi.org/10.1007/s00024-018-2065-9>
- Heidbach, O., Rajabi, M., Cui, X., Fuchs, K., Müller, B., Reinecker, J., et al. (2018). The World Stress Map database release 2016: Crustal stress pattern across scales. *Tectonophysics*, 744, 484–498. <https://doi.org/10.1016/j.tecto.2018.07.007>
- Hennig, J., Hall, R., Forster, M. A., Kohn, B. P., & Lister, G. S. (2017). Rapid cooling and exhumation as a consequence of extension and crustal thinning: Inferences from the Late Miocene to Pliocene Palu Metamorphic Complex, Sulawesi, Indonesia. *Tectonophysics*, 712, 600–622. <https://doi.org/10.1016/j.tecto.2017.06.025>
- Hooper, A., Pietrzak, J., Simons, W., Cui, H., Riva, R., Naeije, M., et al. (2013). Importance of horizontal seafloor motion on tsunami height for the 2011 $M_w = 9.0$ Tohoku-Oki earthquake. *Earth and Planetary Science Letters*, 361, 469–479. <https://doi.org/10.1016/j.epsl.2012.11.013>
- Hooper, A., Segall, P., Johnson, K., & Rubinstein, J. (2002). Reconciling seismic and geodetic models of the 1989 Kilauea south flank earthquake. *Geophysical Research Letters*, 29(22), 19-1–19-4. <https://doi.org/10.1029/2002gl016156>
- Hornbach, M. J., Braudy, N., Briggs, R. W., Cormier, M.-H., Davis, M. B., Diebold, J. B., et al. (2010). High tsunami frequency as a result of combined strike-slip faulting and coastal landslides. *Nature Geoscience*, 3(11), 783–788. <https://doi.org/10.1038/ngeo975>
- Imamura, F., Synolakis, C. E., Gica, E., Titov, V., Listanco, E., & Lee, H. J. (1995). Field survey of the 1994 Mindoro Island, Philippines tsunami. *Pure and Applied Geophysics*, 144(3–4), 875–890. <https://doi.org/10.1007/BF00874399>
- Jamelot, A., Gailler, A., Heinrich, P., Vallage, A., & Champenois, J. (2019). Tsunami simulations of the Sulawesi M_w 7.5 event: Comparison of seismic sources issued from a tsunami warning context versus post-event finite source. *Pure and Applied Geophysics*, 176(8), 3351–3376. <https://doi.org/10.1007/s00024-019-02274-5>
- Jaya, A., Nishikawa, O., & Jumadil, S. (2019). Distribution and morphology of the surface ruptures of the 2018 Donggala–Palu earthquake, central Sulawesi, Indonesia. *Earth Planets and Space*, 71(1), 1–13. <https://doi.org/10.1186/s40623-019-1126-3>
- Jung, H. S., Won, J. S., & Kim, S. W. (2009). An improvement of the performance of multiple-aperture SAR interferometry (MAI). *IEEE Transactions on Geoscience and Remote Sensing*, 47(8), 2859–2869. <https://doi.org/10.1109/TGRS.2009.2016554>
- Katili, J. A. (1970). Large transcurrent faults in Southeast Asia with special reference to Indonesia. *Geologische Rundschau*, 59(2), 581–600. <https://doi.org/10.1007/bf01823809>
- King, D. (2015). Tsunami hazard, assessment and risk in Aotearoa–New Zealand: A systematic review AD 1868–2012. *Earth-Science Reviews*, 145, 25–42. <https://doi.org/10.1016/j.earscirev.2015.02.004>

- Klinger, Y. (2010). Relation between continental strike-slip earthquake segmentation and thickness of the crust. *Journal of Geophysical Research*, 115(B7), B07306. <https://doi.org/10.1029/2009jb006550>
- Laigle, M., Becel, A., de Voogd, B., Hirn, A., Taymaz, T., Ozalaybey, S., et al. (2008). A first deep seismic survey in the Sea of Marmara: Deep basins and whole crust architecture and evolution. *Earth and Planetary Science Letters*, 270(3–4), 168–179. <https://doi.org/10.1016/j.epsl.2008.02.031>
- Latcharot, P., Suppasri, A., Imamura, F., Aytore, B., & Yalçiner, A. C. (2016). Possible worst-case tsunami scenarios around the Marmara Sea from combined earthquake and landslide sources. *Pure and Applied Geophysics*, 173(12), 3823–3846. <https://doi.org/10.1007/s00024-016-1411-z>
- Lee, S.-J., Wong, T.-P., Lin, T.-C., & Liu, T.-Y. (2019). Complex triggering supershear rupture of the 2018 M_w 7.5 Palu, Indonesia, earthquake determined from teleseismic source inversion. *Seismological Research Letters*, 90(6), 2111–2120. <https://doi.org/10.1785/0220190111>
- Leeuwen, T. M. V., & Muhandjo (2005). Stratigraphy and tectonic setting of the Cretaceous and Paleogene volcanic-sedimentary successions in northwest Sulawesi, Indonesia: Implications for the Cenozoic evolution of Western and Northern Sulawesi. *Journal of Asian Earth Sciences*, 25(3), 481–511. <https://doi.org/10.1016/j.jseas.2004.05.004>
- Lettis, W., Bachhuber, J., Witter, R., Brankman, C., Randolph, C., Barka, A., & Kaya, A. (2002). Influence of releasing step-overs on surface fault rupture and fault segmentation: Examples from the 17 August 1999 Izmit earthquake on the North Anatolian fault, Turkey. *Bulletin of the Seismological Society of America*, 92(1), 19–42. <https://doi.org/10.1785/0120000808>
- Li, Q., Zhao, B., Tan, K., & Xu, W. (2020). Two main rupture stages during the 2018 magnitude 7.5 Sulawesi earthquake. *Geophysical Journal International*, 221(3), 1873–1882. <https://doi.org/10.1093/gji/ggaa115>
- Liu, P., Higuera, P., Husrin, S., Prasetya, G., Prihantono, J., Diastomo, H., et al. (2020). Coastal landslides in Palu bay during 2018 Sulawesi earthquake and tsunami. *Landslides*, 17(9), 2085–2098. <https://doi.org/10.1007/s10346-020-01417-3>
- Maeda, T., & Furumura, T. (2013). FDM simulation of seismic waves, ocean acoustic waves, and tsunamis based on tsunami-coupled equations of motion. *Pure and Applied Geophysics*, 170(1), 109–127. <https://doi.org/10.1007/s00024-011-0430-z>
- Mann, P. (2007). Global catalogue, classification and tectonic origins of restraining-and releasing bends on active and ancient strike-slip fault systems. *Geological Society, London, Special Publications*, 290(1), 13–142. <https://doi.org/10.1144/sp290.2>
- McHugh, C. M., Braudy, N., Çağatay, M. N., Sorlien, C., Cormier, M.-H., Seeber, L., & Henry, P. (2014). Seafloor fault ruptures along the North Anatolia fault in the Marmara Sea, Turkey: Link with the adjacent basin turbidite record. *Marine Geology*, 353, 65–83. <https://doi.org/10.1016/j.margeo.2014.03.005>
- McHugh, C. M., Seeber, L., Cormier, M.-H., & Hornbach, M. (2014). Submarine Paleoseismology along populated transform boundaries: The Enriquillo-plantain-garden fault, Canal du Sud, Haiti, and the north Anatolian fault, Marmara Sea, Turkey. *Oceanography*, 27(2), 118–131. <https://doi.org/10.5670/oceanog.2014.47>
- Michel, R., Avouac, J. P., & Taboury, J. (1999). Measuring near field coseismic displacements from SAR images: Application to the Landers earthquake. *Geophysical Research Letters*, 26(19), 3017–3020. <https://doi.org/10.1029/1999GL900524>
- Mikami, T., Shibayama, T., Esteban, M., Takabatake, T., Nakamura, R., Nishida, Y., et al. (2019). Field survey of the 2018 Sulawesi tsunami: Inundation and run-up heights and damage to coastal communities. *Pure and Applied Geophysics*, 176(8), 3291–3304. <https://doi.org/10.1007/s00024-019-02258-5>
- Muhari, A., Imamura, F., Arikawa, T., Hakim, A. R., & Afriyanto, B. (2018). Solving the puzzle of the September 2018 Palu, Indonesia, tsunami mystery: Clues from the tsunami waveform and the initial field survey data. *Journal of Disaster Research*, 13(Scientific Communication), sc20181108. <https://doi.org/10.20965/jdr.2018.sc20181108>
- Nakata, K., Katsumata, A., & Muhari, A. (2020). Submarine landslide source models consistent with multiple tsunami records of the 2018 Palu tsunami, Sulawesi, Indonesia. *Earth Planets and Space*, 72, 1–16. <https://doi.org/10.1186/s40623-020-01169-3>
- Natawidjaja, D. H., Daryono, M. R., Prasetya, G., Liu, P. L., Hananto, N. D., Kongko, W., et al. (2020). The 2018 M_w 7.5 Palu supershear earthquake ruptures geological fault's multi-segment separated by large bends: Results from integrating field measurements, LiDAR, swath bathymetry, and seismic-reflection data. *Geophysical Journal International*, 224, 985–1002. <https://doi.org/10.1093/gji/ggaa498>
- Nijholt, N., Simons, W., Efendi, J., Sarsito, D., & Riva, R. (2021). A transient in surface motions dominated by deep afterslip subsequent to a shallow supershear earthquake: The 2018 M_w 7.5 Palu Case. *Geochemistry, Geophysics, Geosystems*, 22(4), e2020GC009491. <https://doi.org/10.1029/2020GC009491>
- Oglesby, D. D. (2005). The dynamics of strike-slip step-overs with linking dip-slip faults. *Bulletin of the Seismological Society of America*, 95(5), 1604–1622. <https://doi.org/10.1785/0120050058>
- Ohmachi, T., Tsukiyama, H., & Matsumoto, H. (2001). Simulation of tsunami induced by dynamic displacement of seabed due to seismic faulting. *Bulletin of the Seismological Society of America*, 91(6), 1898–1909. <https://doi.org/10.1785/0120000074>
- Okada, Y. (1985). Surface deformation due to shear and tensile faults in a half-space. *Bulletin of the Seismological Society of America*, 75(4), 1135–1154. <https://doi.org/10.1785/bssa0750041135>
- Omira, R., Dogan, G., Hidayat, R., Husrin, S., Prasetya, G., Annunziato, A., et al. (2019). The September 28th, 2018, tsunami in Palu-Sulawesi, Indonesia: A post-event field survey. *Pure and Applied Geophysics*, 176(4), 1379–1395. <https://doi.org/10.1007/s00024-019-02145-z>
- Özaksoy, V., Emre, Ö., Yıldırım, C., Doğan, A., Özalp, S., & Tokay, F. (2010). Sedimentary record of late Holocene seismicity and uplift of Hersek restraining bend along the North Anatolian Fault in the Gulf of İzmit. *Tectonophysics*, 487(1–4), 33–45. <https://doi.org/10.1016/j.tecto.2010.03.006>
- Öztürk, H., Koral, H., & Geist, E. (2000). Intra-basinal water movements induced by faulting: The August 17, 1999, Gölcük (İzmit Bay) earthquake ($M_w = 7.4$). *Marine Geology*, 170(3–4), 263–270. [https://doi.org/10.1016/S0025-3227\(00\)00090-6](https://doi.org/10.1016/S0025-3227(00)00090-6)
- Pakoksung, K., Suppasri, A., Imamura, F., Athanasius, C., Omang, A., & Muhari, A. (2019). Simulation of the submarine landslide Tsunami on 28 September 2018 in Palu Bay, Sulawesi Island, Indonesia, using a two-layer model. *Pure and Applied Geophysics*, 176(8), 3323–3350.
- Patria, A., & Putra, P. S. (2020). Development of the Palu–Koro fault in NW Palu valley, Indonesia. *Geoscience Letters*, 7(1), 1–11. <https://doi.org/10.1186/s40562-020-0150-2>
- Pelinovsky, E., Yuliadi, D., Prasetya, G., & Hidayat, R. (1997). The 1996 Sulawesi tsunami. *Natural Hazards*, 16(1), 29–38. <https://doi.org/10.1023/a:1007904610680>
- Poupardin, A., Calais, E., Heinrich, P., Hébert, H., Rodriguez, M., Leroy, S., et al. (2020). Deep submarine landslide contribution to the 2010 Haiti Earthquake Tsunami. *Natural Hazards and Earth System Sciences*, 20(7), 2055–2065. <https://doi.org/10.5194/nhess-2019-388>
- Prasetya, G., De Lange, W., & Healy, T. (2001). The Makassar strait tsunamigenic region, Indonesia. *Natural Hazards*, 24(3), 295–307. <https://doi.org/10.1023/a:1012297413280>
- Putra, P. S., Aswan, A., Maryunani, K. A., Yulianto, E., & Kongko, W. (2019). Field survey of the 2018 Sulawesi Tsunami deposits. *Pure and Applied Geophysics*, 176(6), 1–11. <https://doi.org/10.1007/s00024-019-02181-9>
- Rabinovich, A. B., Thomson, R. E., Titov, V. V., Stephenson, F. E., & Rogers, G. C. (2008). Locally generated tsunamis recorded on the coast of British Columbia. *Atmosphere-Ocean*, 46(3), 343–360. <https://doi.org/10.3137/ao.460304>

- Ragon, T., & Simons, M. (2021). Accounting for uncertain 3-D elastic structure in fault slip estimates. *Geophysical Journal International*, 224(2), 1404–1421. <https://doi.org/10.1093/gji/ggaa526>
- Ribot, M., Klinger, Y., Jónsson, S., Avsar, U., Pons-Branchu, E., Matrau, R., & Mallon, F. L. (2021). Active faults' geometry in the Gulf of Aqaba, southern Dead Sea Fault, illuminated by multibeam bathymetric data. *Tectonics*, 40(4), e2020TC006443. <https://doi.org/10.1029/2020tc006443>
- Roberts, K. J., Pringle, W. J., & Westerink, J. J. (2019). OceanMesh2D 1.0: MATLAB-based software for two-dimensional unstructured mesh generation in coastal ocean modeling. *Geoscientific Model Development*, 12(5), 1847–1868. <https://doi.org/10.5194/gmd-12-1847-2019>
- Rosen, P. A., Hensley, S., Zebker, H. A., Webb, F. H., & Fielding, E. J. (1996). Surface deformation and coherence measurements of Kilauea Volcano, Hawaii, from SIR-C radar interferometry. *Journal of Geophysical Research*, 101(E10), 23109–23125. <https://doi.org/10.1029/96JE01459>
- Sassa, S., & Takagawa, T. (2019). Liquefied gravity flow-induced tsunami: First evidence and comparison from the 2018 Indonesia Sulawesi earthquake and tsunami disasters. *Landslides*, 16(1), 195–200. <https://doi.org/10.1007/s10346-018-1114-x>
- Schambach, L., Grilli, S., & Tappin, D. (2020). New high-resolution modeling of the 2018 Palu tsunami, based on supershear earthquake mechanisms and mapped coastal landslides, supports a dual source. *Frontiers of Earth Science*, 8, 627. <https://doi.org/10.3389/feart.2020.598839>
- Sepúlveda, I., Haase, J. S., Carvajal, M., Xu, X., & Liu, P. L. (2020). Modeling the sources of the 2018 Palu, Indonesia, tsunami using videos from social media. *Journal of Geophysical Research: Solid Earth*, 125(3), e2019JB018675. <https://doi.org/10.1029/2019JB018675>
- Shimozono, T., Cui, H., Pietrzak, J., Fritz, H., Okayasu, A., & Hooper, A. (2014). Short wave amplification and extreme runup by the 2011 Tohoku tsunami. *Pure and Applied Geophysics*, 171(12), 3217–3228. <https://doi.org/10.1007/s00024-014-0803-1>
- Socquet, A., Hollingsworth, J., Pathier, E., & Bouchon, M. (2019). Evidence of supershear during the 2018 magnitude 7.5 Palu earthquake from space geodesy. *Nature Geoscience*, 12(3), 192–199. <https://doi.org/10.1038/s41561-018-0296-0>
- Socquet, A., Simons, W., Vigny, C., McCaffrey, R., Subarya, C., Sarsito, D., et al. (2006). Microblock rotations and fault coupling in SE Asia triple junction (Sulawesi, Indonesia) from GPS and earthquake slip vector data. *Journal of Geophysical Research*, 111(B8), B08409. <https://doi.org/10.1029/2005jb003963>
- Sotiris, V., Athanassios, G., Varvara, T., & Aggeliki, B. (2018). A preliminary report on the M7.5 Palu 2018 earthquake co-seismic ruptures and landslides using image correlation techniques on optical satellite data. Report submitted to EMSC on 19 October 2018 12:00 UTC. <https://doi.org/10.5281/zenodo.1467128>
- Stevens, C., McCaffrey, R., Bock, Y., Genrich, J., Subarya, C., Puntodewo, S., et al. (1999). Rapid rotations about a vertical axis in a collisional setting revealed by the Palu fault, Sulawesi, Indonesia. *Geophysical Research Letters*, 26(17), 2677–2680. <https://doi.org/10.1029/1999gl008344>
- Supendi, P., Nugraha, A. D., Widiyantoro, S., Pesicek, J. D., Thurber, C., Abdullah, C., et al. (2020). Relocated aftershocks and background seismicity in eastern Indonesia shed light on the 2018 Lombok and Palu earthquake sequences. *Geophysical Journal International*, 221(3), 1845–1855. <https://doi.org/10.1093/gji/ggaa118>
- Switzer, A. D., Majewski, J. M., Guan, R. Y., Benazir, B., Meilianda, E., Parham, P. R., et al. (2019). The tsunami deposits of the September 28, 2018 Palu earthquake, Sulawesi, Indonesia. In *Geophysical research abstracts, EGU2019-6290* (Vol. 21).
- Syamsidik, B., Umar, M., Margaglio, G., & Fitriyansyah, A. (2019). Post-tsunami survey of the 28 September 2018 tsunami near Palu bay in central Sulawesi, Indonesia: Impacts and challenges to coastal communities. *International Journal of Disaster Risk Reduction*, 38, 101229. <https://doi.org/10.1016/j.ijdrr.2019.101229>
- Takagi, H., Pratama, M. B., Kurobe, S., Esteban, M., Aránguiz, R., & Ke, B. (2019). Analysis of generation and arrival time of landslide tsunami to Palu City due to the 2018 Sulawesi earthquake. *Landslides*, 16(5), 1–9. <https://doi.org/10.1007/s10346-019-01166-y>
- Tanioka, Y., & Satake, K. (1996). Tsunami generation by horizontal displacement of ocean bottom. *Geophysical Research Letters*, 23(8), 861–864. <https://doi.org/10.1029/96gl00736>
- Tchalenko, J. (1970). Similarities between shear zones of different magnitudes. *The Geological Society of America Bulletin*, 81(6), 1625–1640. [https://doi.org/10.1130/0016-7606\(1970\)81\[1625:SBSZOD\]2.0.CO;2](https://doi.org/10.1130/0016-7606(1970)81[1625:SBSZOD]2.0.CO;2)
- ten Brink, U., Wei, Y., Fan, W., Granja-Bruña, J.-L., & Miller, N. (2020). Mysterious tsunami in the Caribbean Sea following the 2010 Haiti earthquake possibly generated by dynamically triggered early aftershocks. *Earth and Planetary Science Letters*, 540, 116269. <https://doi.org/10.1016/j.epsl.2020.116269>
- Tinti, S., Armigliato, A., Manucci, A., Pagnoni, G., Zaniboni, F., Yalçiner, A. C., & Altunok, Y. (2006). The generating mechanisms of the August 17, 1999 Izmit bay (Turkey) tsunami: Regional (tectonic) and local (mass instabilities) causes. *Marine Geology*, 225(1–4), 311–330. <https://doi.org/10.1016/j.margeo.2005.09.010>
- Tobita, M., Murakami, M., Nakagawa, H., Yurai, H., Fujiwara, S., & Rosen, P. A. (2001). 3-D surface deformation of the 2000 Usu eruption measured by matching of SAR images. *Geophysical Research Letters*, 28(22), 4291–4294. <https://doi.org/10.1029/2001GL013329>
- Ulrich, T., Vater, S., Madden, E. H., Behrens, J., van Dinther, Y., Van Zelst, I., et al. (2019). Coupled, physics-based modeling reveals earthquake displacements are critical to the 2018 Palu, Sulawesi Tsunami. *Pure and Applied Geophysics*, 176(10), 4069–4109. <https://doi.org/10.1007/s00024-019-02290-5>
- USGS. (2018). *Finite fault solution of the M_w 7.5 Palu earthquake, Indonesia*. US Geological Survey. Retrieved from <https://earthquake.usgs.gov/earthquakes/eventpage/us1000h3p4/finite-fault>
- Van Laarhoven, P. J., & Aarts, E. H. (1987). Simulated annealing. In *Simulated annealing: Theory and applications* (pp. 7–15). Springer.
- Walpersdorf, A., Rangin, C., & Vigny, C. (1998). GPS compared to long-term geologic motion of the north arm of Sulawesi. *Earth and Planetary Science Letters*, 159(1–2), 47–55. [https://doi.org/10.1016/s0012-821x\(98\)00056-9](https://doi.org/10.1016/s0012-821x(98)00056-9)
- Walpersdorf, A., Vigny, C., Subarya, C., & Manurung, P. (1998). Monitoring of the Palu-Koro fault (Sulawesi) by GPS. *Geophysical Research Letters*, 25(13), 2313–2316. <https://doi.org/10.1029/98gl01799>
- Wang, H., & Wright, T. (2012). Satellite geodetic imaging reveals internal deformation of western Tibet. *Geophysical Research Letters*, 39(7), 7303. <https://doi.org/10.1029/2012gl015222>
- Wang, Y., Feng, W., Chen, K., & Samsonov, S. (2019). Source characteristics of the 28 September 2018 M_w 7.4 Palu, Indonesia, earthquake derived from the advanced land observation satellite 2 data. *Remote Sensing*, 11(17), 1999. <https://doi.org/10.3390/rs11171999>
- Watkinson, I. M., & Hall, R. (2017). Fault systems of the eastern Indonesian triple junction: Evaluation of quaternary activity and implications for seismic hazards. *Geological Society, London, Special Publications*, 441(1), 71–120. <https://doi.org/10.1144/sp441.8>
- Watkinson, I. M., & Hall, R. (2019). Impact of communal irrigation on the 2018 Palu earthquake-triggered landslides. *Nature Geoscience*, 12(11), 940–945. <https://doi.org/10.1038/s41561-019-0448-x>
- Widiyanto, W., Santoso, P. B., Hsiao, S.-C., & Imananta, R. T. (2019). Post-event field survey of 28 September 2018 Sulawesi earthquake and tsunami. *Natural Hazards and Earth System Sciences*, 19(12), 2781–2794. <https://doi.org/10.5194/nhess-19-2781-2019>
- Williamson, A. L., Melgar, D., Xu, X., & Milliner, C. (2020). The 2018 Palu tsunami: Coeval landslide and coseismic sources. *Seismological Research Letters*, 91(6), 3148–3160. <https://doi.org/10.1785/0220200009>
- Wilson, P., Rais, J., Reigber, C., Reinhart, E., Ambrosius, B., Le Pichon, X., et al. (1998). Study provides data on active plate tectonics in South-east Asia region. *Eos, Transactions American Geophysical Union*, 79(45), 545–549. <https://doi.org/10.1029/98eo00398>

- Wright, T. J., Parsons, B. E., & Lu, Z. (2004). Toward mapping surface deformation in three dimensions using InSAR. *Geophysical Research Letters*, *31*(1), L01607. <https://doi.org/10.1029/2003gl018827>
- Wu, D., Ren, Z., Liu, J., Chen, J., Guo, P., Yin, G., et al. (2020). Coseismic surface rupture during the 2018 M_w 7.5 Palu earthquake, Sulawesi Island, Indonesia. *GSA Bulletin*, *133*(5–6), 1157–1166. <https://doi.org/10.1130/b35597.1>
- Yalçiner, A. C., Alpar, B., Altunok, Y., Özbay, I., & Imamura, F. (2002). Tsunamis in the Sea of Marmara: Historical documents for the past, models for the future. *Marine Geology*, *190*(1–2), 445–463. [https://doi.org/10.1016/S0025-3227\(02\)00358-4](https://doi.org/10.1016/S0025-3227(02)00358-4)
- Yalçiner, A. C., Hidayat, R., Husrin, S., Prasetya, G., Annunziato, A., Doğan, G. G., et al. (2018). The 28th September 2018 Palu Earthquake and Tsunami ITST 07-11 November 2018 Post Tsunami Field Survey Report (Short). Retrieved from http://itic.ioc-unesco.org/images/stories/its_tsunami_survey/itst_palu/ITST-Nov-7-11-Short-Survey-Report-due-on-November-23-2018.pdf
- Yolsal-Çevikbilen, S., & Taymaz, T. (2019). Source characteristics of the 28 September 2018 M_w 7.5 Palu-Sulawesi, Indonesia (SE Asia) earthquake based on inversion of teleseismic bodywaves. *Pure and Applied Geophysics*, *176*(10), 4111–4126. <https://doi.org/10.1007/s00024-019-02294-1>
- Zhang, Y., Chen, Y.-T., & Feng, W. (2019). Complex multiple-segment ruptures of the 28 September 2018, Sulawesi, Indonesia, earthquake. *Science Bulletin*, *64*(10), 650–652. <https://doi.org/10.1016/j.scib.2019.04.018>

References From the Supporting Information

- Altamimi, Z., Rebischung, P., Métivier, L., & Collilieux, X. (2016). ITRF2014: A new release of the International Terrestrial Reference Frame modeling nonlinear station motions. *Journal of Geophysical Research: Solid Earth*, *121*(8), 6109–6131. <https://doi.org/10.1002/2016jb013098>
- Amev, R., Hooper, A., & Walters, R. (2018). A Bayesian method for incorporating self-similarity into earthquake slip inversions. *Journal of Geophysical Research: Solid Earth*, *123*(7), 6052–6071. <https://doi.org/10.1029/2017jb015316>
- Baran, I., Stewart, M. P., Kampes, B. M., Perski, Z., & Lilly, P. (2003). A modification to the Goldstein radar interferogram filter. *IEEE Transactions on Geoscience and Remote Sensing*, *41*(9), 2114–2118. <https://doi.org/10.1109/TGRS.2003.817212>
- Bertiger, W., Desai, S. D., Haines, B., Harvey, N., Moore, A. W., Owen, S., & Weiss, J. P. (2010). Single receiver phase ambiguity resolution with GPS data. *Journal of Geodesy*, *84*(5), 327–337. <https://doi.org/10.1007/s00190-010-0371-9>
- Bos, M., & Scherneck, H. (2014). Onsala space observatory. Retrieved from <http://holt.oso.chalmers.se/loading>. Accessed 1Mar2018
- Goldstein, R. M., & Werner, C. L. (1998). Radar interferogram filtering for geophysical applications. *Geophysical Research Letters*, *25*(21), 4035–4038. <https://doi.org/10.1029/1998GL900033>
- Gomba, G., Parizzi, A., De Zan, F., Eineder, M., & Bamler, R. (2016). Toward operational compensation of ionospheric effects in SAR interferograms: The split-spectrum method. *IEEE Transactions on Geoscience and Remote Sensing*, *54*(3), 1446–1461. <https://doi.org/10.1109/TGRS.2015.2481079>
- Hastings, W. K. (1970). Monte Carlo sampling methods using Markov chains and their applications.
- Johnston, G., Riddell, A., & Hausler, G. (2017). The international GNSS service. In P. J. G. Teunissen & O. Montenbruck (Eds.), *Springer handbook of global navigation satellite systems* (pp. 967–982). Springer. <https://doi.org/10.1007/978-3-319-42928-1>
- JPL. (2017). GNSS-inferred positioning system and orbit analysis simulation software (GIPSY-OASIS).
- Kobayashi, T., Takada, Y., Furuya, M., & Murakami, M. (2009). Locations and types of ruptures involved in the 2008 Sichuan earthquake inferred from SAR image matching. *Geophysical Research Letters*, *36*(7), 1–5. <https://doi.org/10.1029/2008GL036907>
- Maerten, F., Resor, P., Pollard, D., & Maerten, L. (2005). Inverting for slip on three-dimensional fault surfaces using angular dislocations. *Bulletin of the Seismological Society of America*, *95*(5), 1654–1665. <https://doi.org/10.1785/0120030181>
- Metropolis, N., Rosenbluth, A. W., Rosenbluth, M. N., Teller, A. H., & Teller, E. (1953). Equation of state calculations by fast computing machines. *The Journal of Chemical Physics*, *21*(6), 1087–1092. <https://doi.org/10.1063/1.1699114>
- Morishita, Y., Kobayashi, T., & Yarai, H. (2016). Three-dimensional deformation mapping of a dike intrusion event in Sakurajima in 2015 by exploiting the right-and left-looking ALOS-2 InSAR. *Geophysical Research Letters*, *43*(9), 4197–4204. <https://doi.org/10.1002/2016gl068293>
- Mustafar, M. A., Simons, W. J., Tongkul, F., Satirapod, C., Omar, K. M., & Visser, P. N. (2017). Quantifying deformation in North Borneo with GPS. *Journal of Geodesy*, *91*(10), 1241–1259. <https://doi.org/10.1007/s00190-017-1024-z>
- Persson, P.-O., & Strang, G. (2004). A simple mesh generator in MATLAB. *SIAM Review*, *46*(2), 329–345. <https://doi.org/10.1137/s0036144503429121>
- Rebischung, P., & Schmid, R. (2016). IGS14/igs14. Atx: A new framework for the IGS products. In *Agu fall meeting 2016*.
- Simons, W., Socquet, A., Vigny, C., Ambrosius, B., Haji Abu, S., Promthong, C., et al. (2007). A decade of GPS in Southeast Asia: Resolving Sundaland motion and boundaries. *Journal of Geophysical Research*, *112*(B6), B06420. <https://doi.org/10.1029/2005jb003868>
- Supendi, P., Nugraha, A. D., Widiyantoro, S., Abdullah, C. I., Puspito, N. T., Palgunadi, K. H., et al. (2019). Hypocenter relocation of the aftershocks of the M_w 7.5 Palu earthquake (September 28, 2018) and swarm earthquakes of Mamasa, Sulawesi, Indonesia, using the BMKG network data. *Geoscience Letters*, *6*(1), 1–11. <https://doi.org/10.1186/s40562-019-0148-9>
- Vigny, C., Perfettini, H., Walpersdorf, A., Lemoine, A., Simons, W., van Loon, D., et al. (2002). Migration of seismicity and earthquake interactions monitored by GPS in SE Asia triple junction: Sulawesi, Indonesia. *Journal of Geophysical Research*, *107*(B10), ETG-7–ETG-11. <https://doi.org/10.1029/2001jb000377>
- Yamazaki, D., Ikeshima, D., Tawatari, R., Yamaguchi, T., O’Loughlin, F., Neal, J. C., et al. (2017). A high-accuracy map of global terrain elevations. *Geophysical Research Letters*, *44*(11), 5844–5853. <https://doi.org/10.1002/2017gl072874>
- Zumberge, J., Hefflin, M., Jefferson, D., Watkins, M., & Webb, F. (1997). Precise point positioning for the efficient and robust analysis of GPS data from large networks. *Journal of Geophysical Research: Solid Earth*, *102*(B3), 5005–5017. <https://doi.org/10.1029/96jb03860>

Erratum

In the originally published version of this article, the typesetter failed to include Movie S1 in the supporting information. The errors were purely typographical, and the implementation of Movie S1 was unaffected. This may be considered the authoritative version of record.